Measurement 246 (2025) 116693

Contents lists available at ScienceDirect

Measurement

journal homepage: www.elsevier.com/locate/measurement

# 2D temperature distribution reconstruction of steel bars under thermal transient from sequences of occluded infrared images

Vittoria Medici [a,*], Milena Martarelli [a], Paolo Castellini [a], Helmert Van De Kamp [b], Nicola Paone [a]

[a] Università Politecnica Delle Marche – DIISM, Via Brecce Bianche 11, 60130 Ancona, AN, Italy
[b] VDL Weweler Bv, Ecofactorij 10, 7325 WC Apeldoorn, Netherlands

ARTICLE INFO

*Keywords:*
Thermography
Occluded image stitching
High temperature
Steel industry
In-line quality control

ABSTRACT

In-line thermography evaluates surface temperature distributions for quality control. This paper addresses the issue when the thermal imaging camera cannot fully capture a moving component undergoing successive stages of processing with transient thermal behavior. Reconstruction of the 2D temperature distribution requires stitching sequential partial images. When the object is moving and undergoing a thermal transient, simple stitching of sequential images leads to discontinuities and erroneous temperature distribution because the images are framed at different times. The correction of such artifacts is demonstrated using steel bars coming out of an induction furnace as an example. Two strategies are compared: temporal alignment and spatial alignment. Spatial alignment considers cooling relative to the distance from the furnace, requiring knowledge of the transient thermal pattern of the bar. The performance of the method is discussed in terms of effectiveness, uncertainty, and practical implementation.

## 1. Introduction

In today's industrial environments, Zero-Defect Manufacturing emerges to improve the efficiency and effectiveness of production processes [1] and, with the evolution of electronics and computational tools, Non-Destructive Testing (NDT) are increasingly suitable for inline operation. Inline measurements are paramount to identify anomalies and avoid defect propagation through the line. In this context, Non-Destructive Inspection systems (NDIs), as Industry 4.0 enabling technology [2], are employed to detect features in-line at the earliest stages of the manufacturing process. NDIs are required to provide accurate information to be used for data analytics, decision support tools, and business decision-making. To provide valuable information, sources of measurement errors must be detected, quantified, and, if possible, corrected.

NDIs features depend on the nature of the variable to be monitored. If it is necessary to monitor surface temperature distribution, thermographic NDIs are required. The main advantage of thermography is the ability to obtain 2D temperature distributions rather than a point measurement. For example, in [3] thermography is necessary to obtain temperature information along the width of the measuring object. The other advantages are the ability to obtain temperature data on objects at very high temperatures, as in [4], and the ability to acquire infrared radiation emitted by moving objects [5]. According to [6], these advantages render thermography a promising measurement technique in the steel industry. Some steel-industry applications of thermography can be found in [7,8,9]. Thermography can also be a valuable tool for qualitative measurements. When thermomechanical treatments are employed to deform material during manufacturing operations, temperature uniformity is an important feature to evaluate.

Monitoring and optimizing the temperature distribution of steel bars as they exit a furnace is crucial for ensuring product quality and operational efficiency. This study is focused on a thermographic NDI system installed at the exit of an induction furnace that heats steel bars to temperatures above 1400 K. After the induction furnace, the bar enters the descaling unit where it is cooled due to the removal of oxides on the surface using water jets. Next, several stations deal with the deformation of the part. According to [10], temperature measurements are essential for forming processes, to properly deform the bars without producing defects. Thermographic systems are often designed to be installed in-line

* Corresponding author.
*E-mail addresses:* v.medici@pm.univpm.it (V. Medici), m.martarelli@staff.univpm.it (M. Martarelli), p.castellini@staff.univpm.it (P. Castellini), W.van.de.Kamp@vdlweweler.nl (H.V. De Kamp), n.paone@staff.univpm.it (N. Paone).

https://doi.org/10.1016/j.measurement.2025.116693
Received 14 May 2024; Received in revised form 19 November 2024; Accepted 6 January 2025
Available online 7 January 2025

to frame the entire object of measurement [2,8,9,11]. However, in the industrial plant considered in this paper, the thermal camera cannot frame the whole bar acquiring a single thermal image due to the machinery layout, which partially obstructs the field of view of the camera. In fact, the distance between the exit of the induction furnace and the entrance of the descaling unit is intentionally kept short, in order to minimize cooling of the bar. Since the bar length is larger than this distance, the camera can frame it only partially, therefore an image of the whole bar can be reconstructed only by stitching occluded multiple images taken in sequence while the bar moves. The alternative would be to send multiple images without concern for their union, but combining the data into a single piece of information increases the efficiency of the pipeline. According to [12], if the information were to go to an operator, a single information field would increase its efficiency, allowing it to analyze the entire process as a whole and not in scattered parts.

Line scanning is a technique commonly used in imaging for objects in motion [13], sometimes in combination with lasers for defect detection ([14,15]). Line scanning can be achieved by linear cameras or by matrix cameras properly triggered. The sensor captures one line of an image at a time, instead of capturing the entire image in one frame; the resulting image is reconstructed as a series of lines if a trigger signal is available which encodes spatial motion. However, the industrial scenario being examined does not allow a reliable trigger. In fact, variability is observed in the speed of the steel bar being imaged, which moves over a roller conveyor, initially pushed by a rod, then transported by the motorized rollers and all this results in uneven velocity and relative slip between bar and rollers. In a typical scenario, encoders could be used for determining the motion of the object, however, they fail to provide reliable synchronization in space if a slip occurs. Therefore, without accurate synchronization between the motion of the object and the acquisition of line images from the camera, motion blur or geometrical distortion can occur, compromising the quality and accuracy of the reconstructed image. In such conditions it is impossible to ensure the necessary synchronization, leading to the inability to utilize the line scanning cameras effectively.

Therefore, this paper addresses the question of how to recombine thermal images acquired in sequence on a moving bar during a thermal transient, to reconstruct the thermal spatial distribution over its surface. In this application, to reconstruct the steel bar thermal image, first, the two images must be geometrically stitched. Then, due to the cooling of the bar between the two acquisitions, the temperatures must be corrected to compensate for the discontinuity that is present in the proximity of the stitching area without altering the meaning of thermal data. Two approaches have been evaluated and described in this paper: the alignment of the images in time, adding the value of the thermal discontinuity to the whole second image, and the alignment of the images in space, as if line-scanning has been performed. To align the images in space, the cooling of the bar must be monitored. Thermography is often used to monitor heat flows, heating, or cooling of objects, such as in [16]. Therefore, a thermal video showing the complete transition of the bar must be recorded to create a correction model and compensate for the discontinuity.

The issue of image stitching is common in machine vision applications. It is the process of merging images that have overlapping regions to create a single image with a wide field of view and enhanced resolution [17]. Generally, it is based on features-based methods, on the extraction of common descriptors from the images ([18,19,20]), more recent applications are based on deep learning algorithms [21]. The same issue was also addressed with infrared thermal imaging ([22,23,24,25]). However, the stitching of thermal images was treated with thermal images of common applications, not in hostile environments with extremely high temperatures like the one under analysis. For example, these techniques are used to stitch images of UAV systems or in medical applications [26] where temperatures are not extremely high. Specifically, the stitching of thermal images during a thermal transient, which is the challenge of this study, is not addressed in the literature.

The novelty of the approach lies not in the geometric stitching itself, which is well-established in image processing, but in the handling of significant thermal transient due to the extremely high temperatures involved. In typical image stitching applications, the object is often assumed to have a stationary temperature distribution, or temperature changes in time are negligible. However, in this case, the steel bar exhibits substantial variations of temperature in time, driven by rapid cooling as it moves along the conveyor. These thermal transients introduce additional complexity, as the temperature distribution can vary significantly even within short time intervals. This makes it essential to consider not only the spatial alignment but also the temporal dynamics of heat transfer, which our data-driven method addresses by carefully synchronizing the thermal data acquisition with the motion of the bar. This aspect of thermal stitching, accounting for temperature variations in real-time, represents a key innovation that distinguishes our approach from more conventional image stitching techniques used in lower-temperature and stationary environments impacting significantly on thermographic applications in the high temperature metal industry.

The rest of this paper is organized as follows. In Section 2, materials and methods are described, with a particular focus on the use-case and thermographic setup. The proposed reconstruction methodology is described in Section 3, divided into geometric stitching and thermal correction, which in turn is divided into method No.1 (temporal alignment of images) and method No.2 (spatial alignment of thermal data). In Section 4, an analysis of uncertainty sources is presented and then both methodologies are applied to the thermal images, after analyzing their validity. Finally, conclusions are given in Section 5.

## 2. Materials and methods

### 2.1. Use-case

In many industrial applications, achieving a complete view of the thermal distribution across a component is challenging due to the scale, complexity, or accessibility of the object being monitored. Examples include large aerospace components [24], buildings requiring detailed but overall thermal inspections, or even electrical circuits where microscopic lenses are needed to capture fine details. With reference to high temperature industry, this approach can be effectively applied in industries like steel manufacturing, where similar thermal transients occur in the processing of metal sheets, coils, and other flat products such as plates and strips. Our methodology is particularly suited to scenarios where high temperatures introduce significant thermal transients, resulting in non-uniformities that can affect the quality and integrity of the manufacturing process. One such application is the hot forming of metal bars, where the temperatures involved are exceptionally high. In this context, the thermal transients are more pronounced.

In the Ecoline of VDL Weweler bv, trailer suspension arms for truckers and buses are manufactured. The raw material is a parallelepiped-shaped steel bar which must be deformed to achieve the desired final shape. To be deformed the bar must be brought to a high temperature which is realized by heating it up to about 1400 K in an induction furnace (provided by INDUCTION s.r.l.). Many sources influence the uniform heating of the bar in such a production process, such as heat exchange with the rollers carrying the hot component ([27]-[28]), or the oven operation. Therefore, it is good to monitor the heat exchanges and try to model them by placing the focus on the component to be manufactured. Non-uniformity of the heating process could have consequences in the cooling of the bar, so in its deformation. The non-uniformity of the distribution can lead to the non-straightness of the bar and defects in the later stages of the process.

A thermographic NDI system has been installed in-line for this purpose (Fig. 1) to monitor the surface temperature distribution and detect non-uniformity of the heating process. Due to the obstruction of the field of view, the camera cannot frame the full bar length; in fact, the NDI

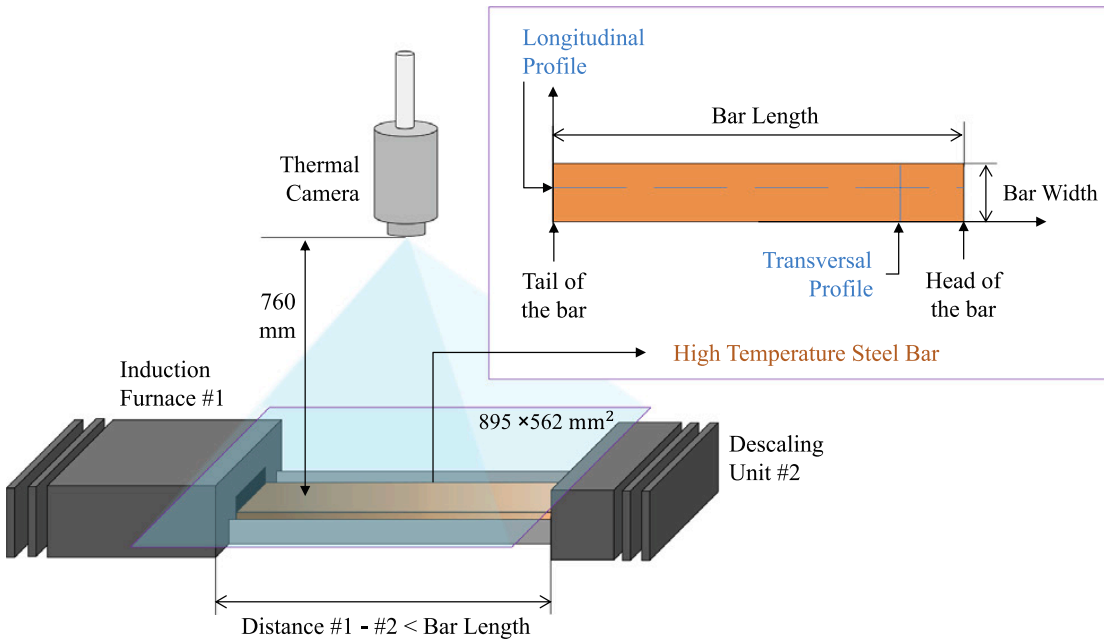


**Fig. 1.** Thermal camera framing the high-temperature steel bar that is leaving the furnace and entering the next station. The distance between the two machines is less than the length of the bar.

acquisition software provides two images (Fig. 2) for each bar: the image of the leading portion of the bar (the head) and the image of the end portion of the bar (the tail).

After these two images are acquired, the processing is done as follows: the bar is cropped by removing the background from both images by rectangle detection, rotation, and image cropping; then the two cropped bar segments are used for geometric reconstruction (Section 3.1). This workflow is represented in the flowchart in Fig. 3.

### 2.2. *Thermal transient phenomenology*

The thermal behavior of the steel bar during the transition from the furnace to the descaling unit involves complex heat transfer dynamics. The bar is initially heated in an induction furnace, where electromagnetic fields induce eddy currents that generate heat within the bar's material. As the bar reaches high temperatures, thermal energy is transmitted throughout its volume by conduction.

As depicted in Fig. 4, the image of the head (blue continuous frame in the top scheme) is captured while the tail of the bar is still inside the furnace, which means it continues to absorb heat. At this stage, also the part of the bar outside the furnace (head) continues to heat up because of the conduction from the part of the bar (tail) that is still inside the furnace. Simultaneously, the part of the bar outside of the furnace (head) dissipates heat through convection in the air and radiation. When a small portion of the head has exited the furnace, the heat dissipated by the bar is still less than the heat being introduced, then the temperature values continue to increase (see data reported in Fig. 4, bottom plot). When a larger length of the bar is outside, the thermal energy introduced by the furnace and the energy dissipated is balanced, and subsequently, the dissipated energy exceeds the incoming energy, leading to the cooling of the bar. The bar starts to cool down from the point of the plot in Fig. 4 denoted with the asterisk.

The second acquisition (green dashed frame in the top scheme of Fig. 4) occurs when the bar tail is completely out of the furnace. In this case the tail of the whole bar is exposed to the environment while the head has already entered inside the descaling unit, where it is subjected to water sprays. These high-pressure sprays serve to mechanically remove oxides from the steel surface. However, water acts as a cooling medium with a significantly higher heat transfer coefficient than air and absorbing latent heat through evaporation. As a result, the surface temperature of the steel bar in the descaling unit decreases rapidly and significantly lower temperatures occur in the tail image than in the head image.

These physical phenomena in addition to the temporal and spatial disparity between the two image acquisitions, all together, explain the reasons why the simple stitching of the two images introduces an artifact which appear as a thermal discontinuity. The head, still influenced by residual heat from the furnace, exhibits a higher temperature, while the

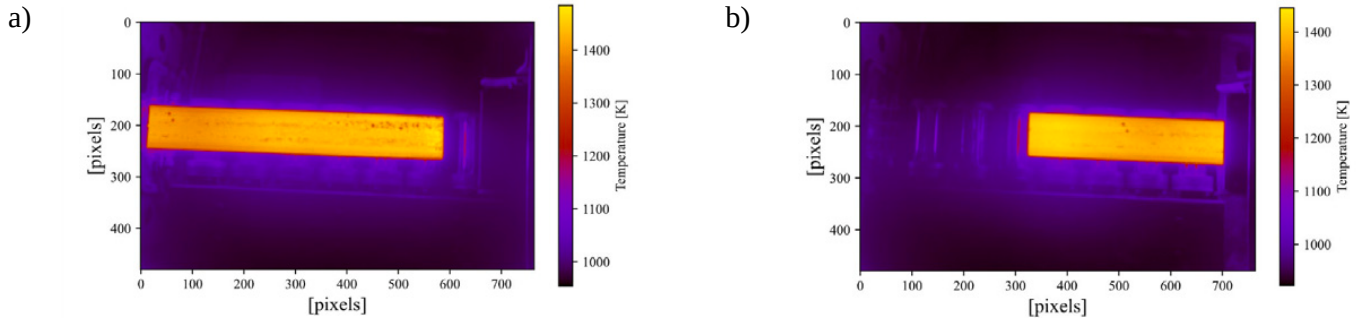


**Fig. 2.** Thermal images acquired at bar transition: a) head image, the tail of the bar is still inside the furnace, b) tail image, the head of the bar is already inside the descaling unit.

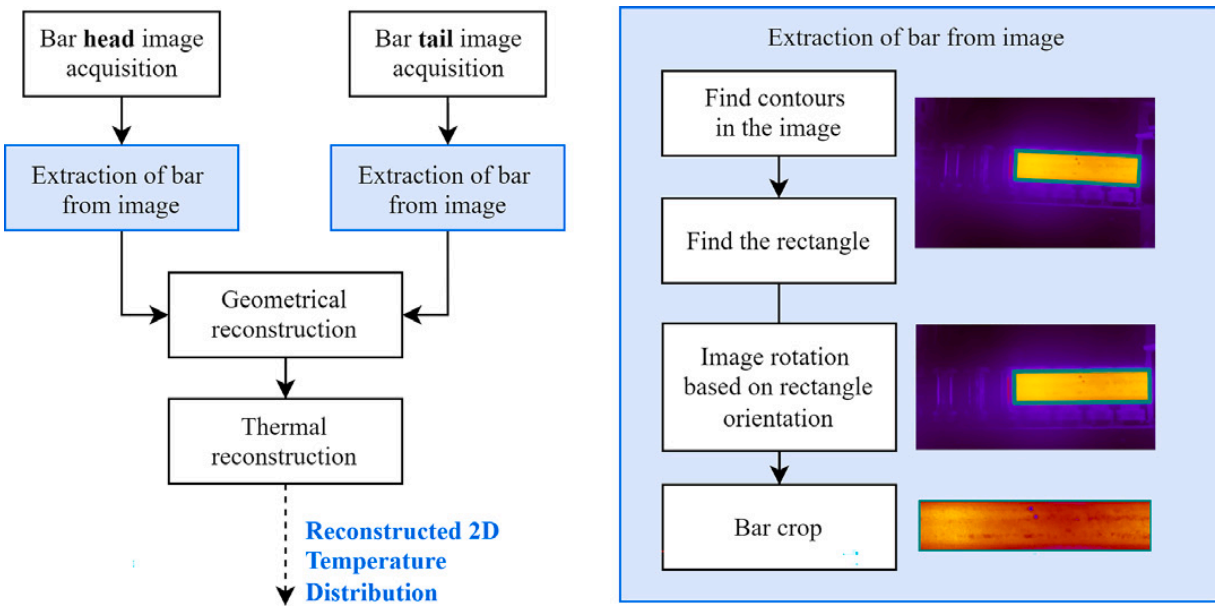


**Fig. 3.** Flowchart of the thermal images processing and 2D Temperature Distribution reconstruction.

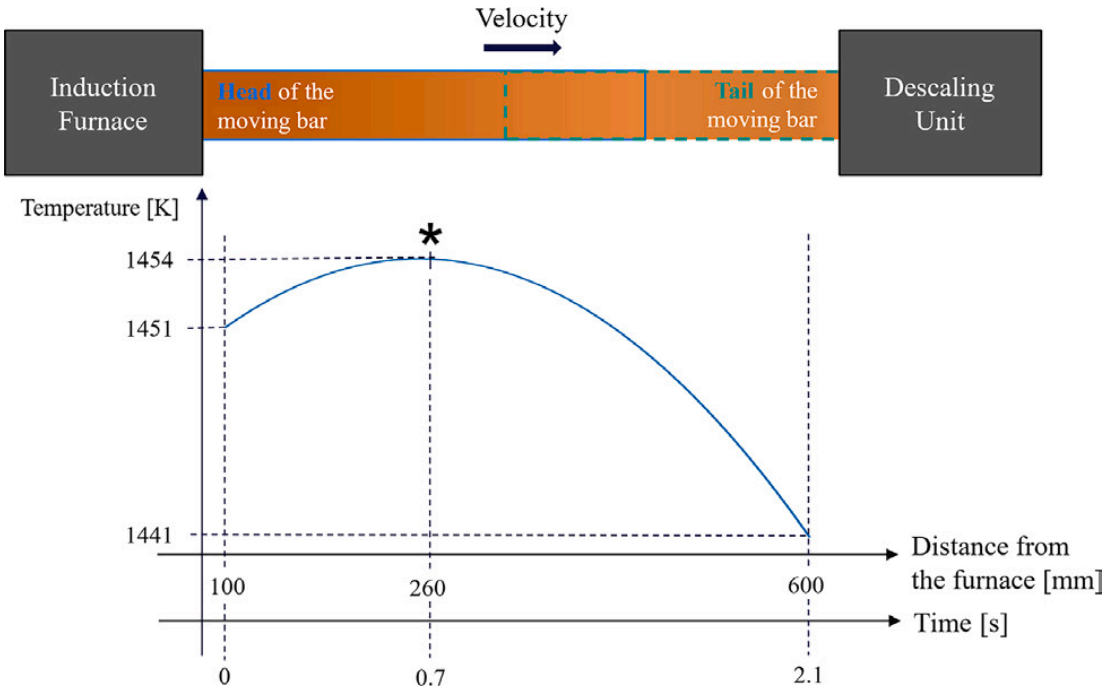


**Fig. 4.** Schematic representation of the steel bar's thermal behavior during its transition from the furnace to the descaling unit.

tail, which is subject to cooling, exhibits a decreasing temperature profile. This thermal discontinuity creates an artifact in the stitched thermal image, potentially leading to false positives in diagnostics. Such artifacts may be mistakenly interpreted as defects in the manufacturing process, compromising the accuracy of any subsequent analysis. Therefore, mitigating or eliminating this discontinuity while maintaining the integrity of the thermal data is crucial for accurate diagnostics.

This paper presents two methodologies to mitigate the thermal discontinuity that will occur when stitching thermal images undergoing a thermal transient. The first methodology focuses on mitigating the thermal disparity by applying a correction that compensates for the cooling of the tail and aligns data in time as if a snapshot was taken. The second methodology, on the other hand, adopts a model of the cooling process to align data in space, each part of the bar acquired at the same position. However, it is not feasible to model the full thermal dynamics of the process, as numerous unknown parameters contribute to the bar's cooling and heating behavior, including factors related to heat loss to the environment, the bar's movement speed, and the exact influence of the water sprays in the descaling unit. Due to these uncertainties and the inherent complexity of the process, it is challenging to construct a purely physics-based model that accurately captures the thermal behavior of the bar at each point in the process.

To address this challenge, the second methodology presented in this paper leverages a data-driven cooling model. This model is constructed based on an analysis of thermographic data obtained from video sequences that capture the complete thermal evolution of the bar as it

transitions from the furnace to the descaling unit. By analyzing these thermal videos, patterns in the cooling behavior can be extracted, as shown in the figure, allowing the model to predict the cooling rates and temperature gradients along the bar more effectively. This data-driven approach compensates for the lack of complete knowledge about the system's physical parameters by using empirical data to approximate the bar's cooling dynamics.

Finally, this paper develops and demonstrates the methodology applying it to steel bars; its demonstration has been done on the real application case to which it was possible to access and install equipment in the production line during normal production. Even if the aspect ratio of a bar is different than that of a slab (bars are slender bodies), the methodology is general and can be applied also to non-slender bodies, whose surface temperature distribution is of interest.

### 2.3. Experimental setup

The thermal camera employed for the acquisition is the Optris PI 1 M model. The spectral range is 0.85 – 1.1 μm, Near InfraRed (NIR). It can detect temperature values in the range 500 – 1800 °C with a CMOS sensor of 764 x 480-pixel resolution. The thermal camera has a Noise Equivalent Differential Temperature (NETD) of about 4 K (for temperature under 1400 °C). NETD is a measure of the signal-to-noise ratio of a detector of thermal radiation, it indicates the minimum temperature difference that is still resolvable by the IR camera. Due to the harsh environment, the thermal camera is housed in a cooling jacket, and it is continuously cooled with water. The thermal camera frames an area of about 895 × 562 $mm^2$ (Fig. 1), therefore its spatial resolution in the object plane is about 1.2 mm/pixel. The distance between the lens and the surface of the framed steel bar is about 760 mm. The experimental setup, which is the NDI installed inline, is shown in Fig. 5.

The emissivity of the bar was set to 0.85 based on experimental tests preliminarily carried out in the laboratory on a blackbody at the same temperature as the steel bar during production.

The thermal camera is controlled via software by an SDK and thermal images are acquired when triggered with a TTL signal provided by the industrial PLC controlling the process. This acquisition software acquires the image of the head and then the image of the tail of the bar, and these images are then read by another software developed in Python, which processes them. Before information about the temperature distribution can be derived, it is necessary to reconstruct the thermal image by stitching them together and correcting the temperature values appropriately.

## 3. Reconstruction methodology

When merging two thermal images undergoing to a thermal transient and acquired at different times to reconstruct the 2D thermal distribution, three dimensions must be considered: two for the position in space (pixel in $x$ and $y$ direction) and the third for the time $t$ across pixels. For each bar, the spatial distribution of temperature is a function of time $T$ ($x$, $y$, $t$). In the case of reconstructing the bar image:

- *Geometric reconstruction* involves stitching the two images to recreate the geometry of the object. Since the bar is a simple rectangle without distinctive features for cross-correlation, an external reference is necessary. This reference could be the length of the bar or its speed during the transition.
- *Thermal reconstruction* entails integrating the thermal profiles, and correction of temperature values. The tail and head of the bar are spatially connected along a transversal profile. In the two images, this profile lies at different distances from the furnace exit, leading to differential cooling rates depending on the time spent outside the furnace.

### 3.1. Geometric reconstruction

Different strategies are possible to geometrically reconstruct the image. In common machine vision applications, geometric matching of images is performed to detect features of objects in the scene [17]. In this application, the steel bar has no features to be monitored during the transition to reconstruct the object image. Some bars show clearly identifiable traces of oxide, but not all. An external parameter is required which could be the speed of the bar or the length of the bar in pixels.

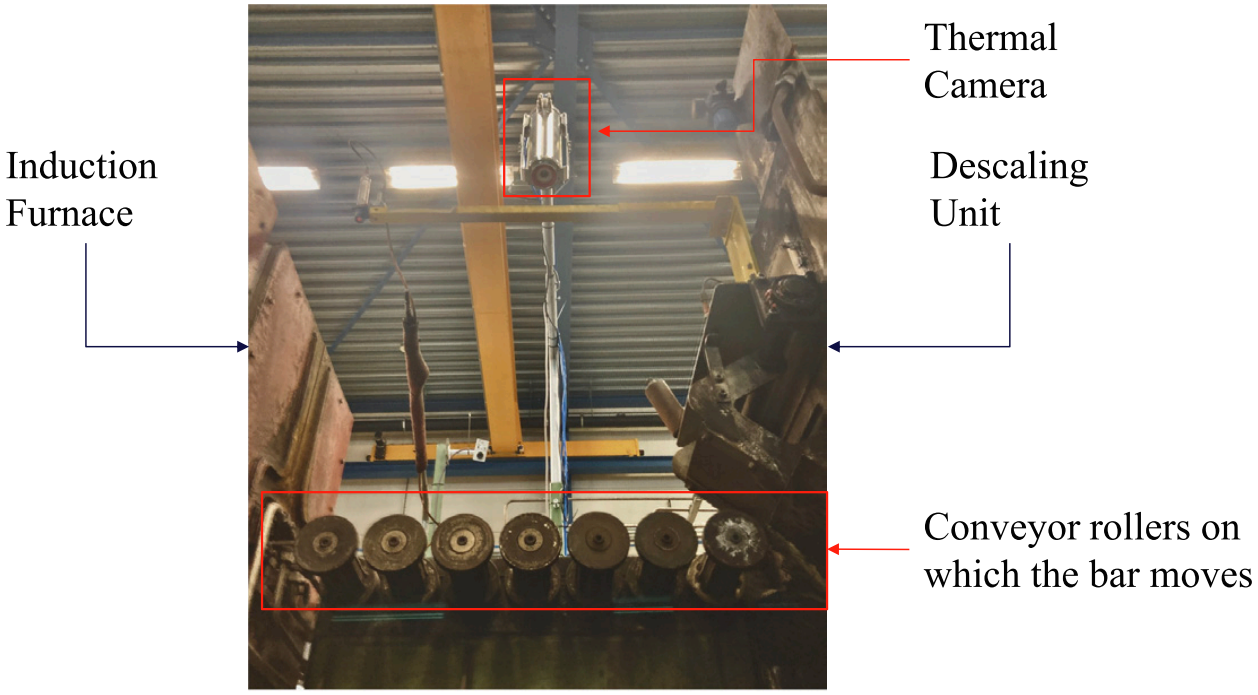


**Fig. 5.** NDI installed in-line.

Given the variability in the speed of the bar during this stage of the process, relying on speed alone as an external parameter for image reconstruction is not feasible. To address this, the adopted strategy leverages the known physical length of the bar, which is provided in millimeters. Using this information, the desired length of the bar in pixels, denoted as $L_d$, is determined through a pixel-to-millimeter ratio, as shown in Eq. (1).

$$L_d\,[\text{pixels}] = \frac{\text{Lenght of the bar [mm]}}{\text{Pixels per mm}} = L_{tail} + L_{head} - L_{overlapping} \quad (1)$$

The geometric reconstruction of the bar's image is carried out by stitching together two segments: the head of length $L_{head}$ and the tail of length $L_{tail}$ of the bar, which are captured at different times during the process, as illustrated in Fig. 2. The two segments are depicted in more detail in Fig. 6.

The two bar segments, extracted from the two images, have a portion in common called the overlapping area, of length $L_{overlapping}$ which can be extracted from Eq. (1). Once defined, to manage this overlap, an arbitrary parameter $k$ is introduced. The parameter $k$ specifies the portion of the tail that will not be considered in the geometric reconstruction. In other words, the tail length used for reconstruction is reduced by this parameter, and it is $L_{tail^*}$. Conversely, the head length used ($L_{head^*}$) for reconstruction consists of the non-overlapping portion of the bar present only in the head image, plus the $k$ portion of the overlapping region (Eq. (2)).

$$L_{head^*} = L_d - (L_{tail} - k) k \in (0, L_{overlapping}) \quad (2)$$

The parameter k plays a crucial role in the geometric reconstruction. Its value must be chosen carefully to ensure that the thermal data from both the head and tail segments align properly, thus minimizing any discontinuities in the temperature distribution. If k is too large or too small, it could introduce errors in the reconstructed thermal profile, leading to inaccurate assessments of the bar's quality. Therefore, the parameter k is optimized based on empirical data.

### 3.2. Thermal reconstruction

After geometric matching, two distinct methodologies are proposed for the thermal reconstruction of the bar and thus to eliminate the discontinuity:

- *Time-alignment of the thermal images* (method no.1)*:* change the values of $T$ in one of the two images to the acquisition time of the other image. This adjustment effectively simulates the scenario where the second image is captured at the time of acquisition of the first image, capturing the state of the object before any significant cooling occurs. In essence, it is akin to taking a snapshot at the exact time of acquisition of the first image, allowing for a comparison at a consistent temporal reference point.
- *Space-alignment of the thermal images* (method no.2)*:* change the values of both images to return all values to the same point in space. This adjustment simulates the scenario where line-scanning is performed at a specific distance from the exit of the furnace.

The two methodologies are better described in 3.2.1 and 3.2.2 subsections.

Processing for thermal alignment is done on a 1D temperature signal obtained by averaging over the bar width the longitudinal profiles of temperature distributions along the bar length (for a clear representation of the longitudinal profiles see the scheme in Fig. 1).

#### 3.2.1. Time-alignment–method n.1

A straightforward thermal reconstruction method that eliminates the

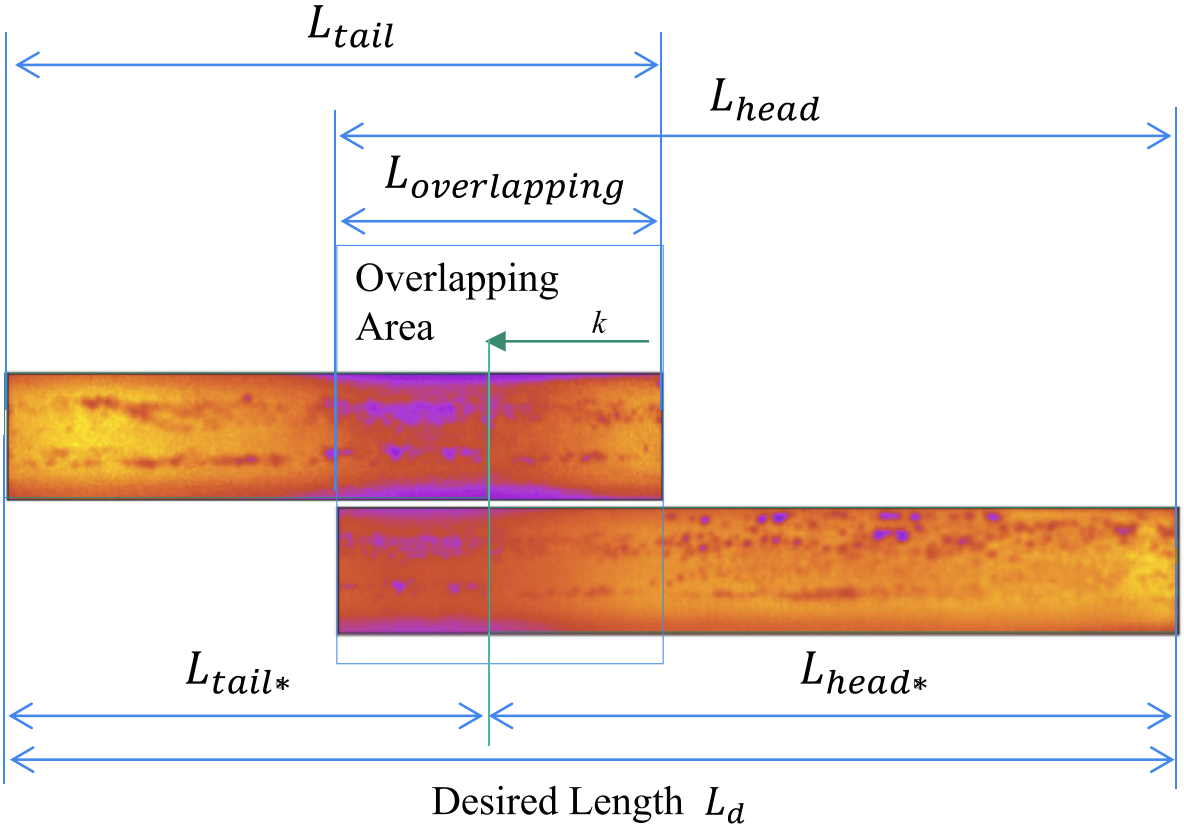


**Fig. 6.** Geometric reconstruction of the bar. Two portions of the bar, which are cropped from different images, must be stitched in order to reconstruct the shape of the bar with the desired length.

discontinuity involves adding the temperature difference value occurring in the x-position where the two thermal images are connected, as evidenced at pixel 222 in Fig. 7, representing the longitudinal thermal profiles of the bar. This adjustment aligns the tail image data (green line in Fig. 7) to the acquisition time of the head image (red line) and transform the tail profile in the yellow line. Conversely, another approach could entail subtracting the temperature difference value from the head image, thus reverting temperature values to the acquisition time of the tail image. This process ensures temporal consistency between the thermal profiles of the head and tail, facilitating seamless integration and analysis. It can be noticed that the difference is calculated on the longitudinal mean profile, so it is not possible to eliminate the discontinuity in all rows or the thermal image. However, this prevents noise from impacting the reconstruction process. The way in which the temperature differences at the discontinuity attenuate along the various rows can be seen in Fig. 9.

The stitched thermal image of the bar before and after this type of alignment is shown in Fig. 8, reporting the thermal distributions overall the entire bar (bottom 2D plots) and a close up on the stitching area (top 3D waterfall plots).

To demonstrate the effectiveness of the proposed methodology in resolving the thermal discontinuity, a comparative analysis of the temperature differences across the stitching boundary was performed. Ideally, this difference should be zero in a noise-free uniform spatial distribution. Specifically, the temperature difference has been evaluated at each row of pixels along the width of the bar at the x-position where the head and tail images are connected. For this analysis, two plots are presented in Fig. 9: one for the original stitched thermal image without any correction and another for the image reconstructed using the described alignment method. These plots represent the difference in temperature between the head and tail images across the disjointed region for each row of pixels. In the plot from the original image with the discontinuity, the temperature differences exhibit significant variation along the stitching boundary, with large deviations observed due to the temporal and spatial disparities between the head and tail images. In contrast, the plot for the reconstructed image shows a substantial reduction in temperature differences along the stitching boundary. The alignment method effectively attenuates the thermal discontinuity, as reflected by a lower and more stable difference profile across the image. The overall average temperature difference decreases significantly, further verifying the success of the alignment in achieving a smoother thermal transition.

By comparing the two plots, it is evident that the temperature differences in the reconstructed image are significantly mitigated compared to the original image. The reduction in the overall mean temperature difference provides quantitative evidence that the method effectively addresses the thermal discontinuity, ensuring a more coherent thermal profile across the bar's length.

### 3.2.2. *Space-alignment – method n.2*

Instead of aligning data over time, it is possible to align the data in space, as if all the points have been acquired at the same distance from the furnace. To do this, the cooling of the bar must be considered.

To evaluate the cooling behavior of the bars, a thermal video has been recorded which shows the complete transition of the bar from the induction furnace to the descaling unit. There are no features to monitor, so areas of dimension 5 x 5 $mm^2$ were selected at known distances from the edges of the bar. The authors selected three areas on the head of the bar and three areas on the tail of the bar. The positions of areas on the head of the bar are shown in Fig. 10.

Starting from the tail, the plot in Fig. 11 shows the trend of the temperatures at the three-selected area at different distance from the edge of the bar. It is important to consider that in this case, the bar is completely outside of the furnace and the head of the bar is already inside the descaling, which cools down the bar. The tail of the bar only cools down.

This trend of temperatures can be used to model the correction curve. First, these curves have been fitted with a second-order polynomial, which is shown in Fig. 5 – b. The quality of the fit is quantified by two metrics: Root Mean Square Error (RMSE) and correlation coefficient R-squared ($R^2$). For the 2nd-order polynomial fit, the RMSE was calculated for all three curves and the maximum RMSE is 0.76 K, indicating the average magnitude of the residuals. In addition, the $R^2$ value, which measures the proportion of the variance of the data explained by the model, is 0.99 for all curves. The correction curve must be used to compensate for the cooling of the bar during the transition. It indicates

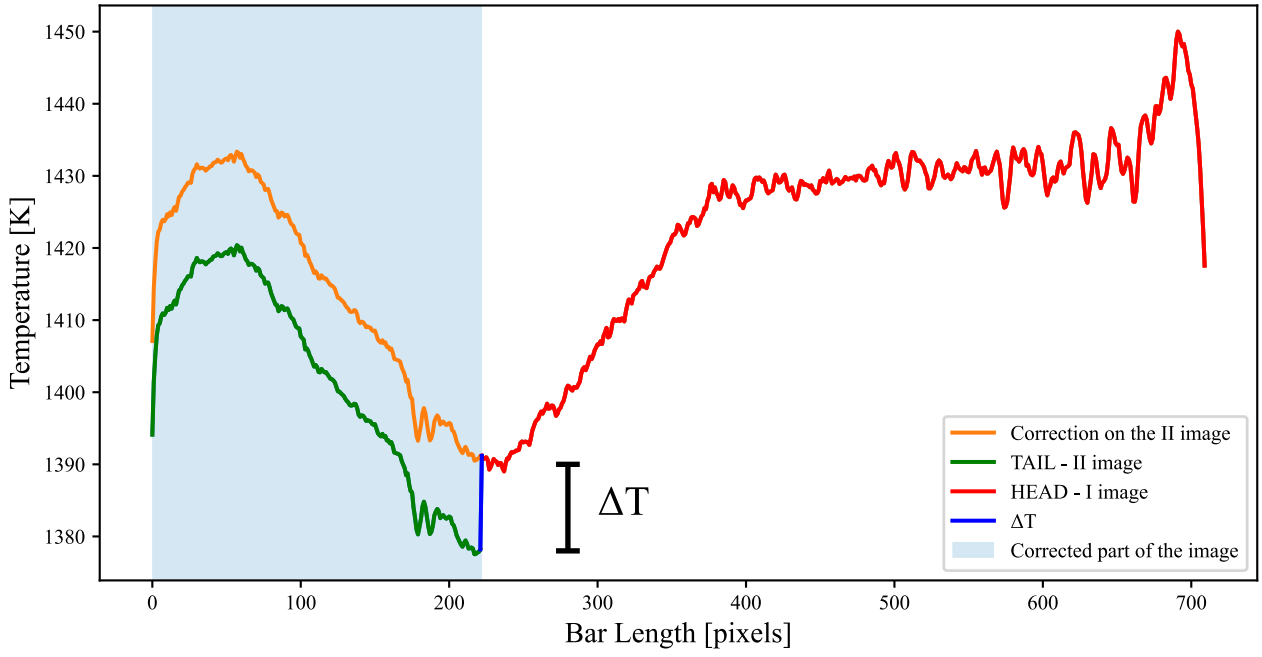


**Fig. 7.** Average Longitudinal Profile before and after the thermal reconstruction: the value of the thermal discontinuity has been added to each pixel of the tail image (orange plot).

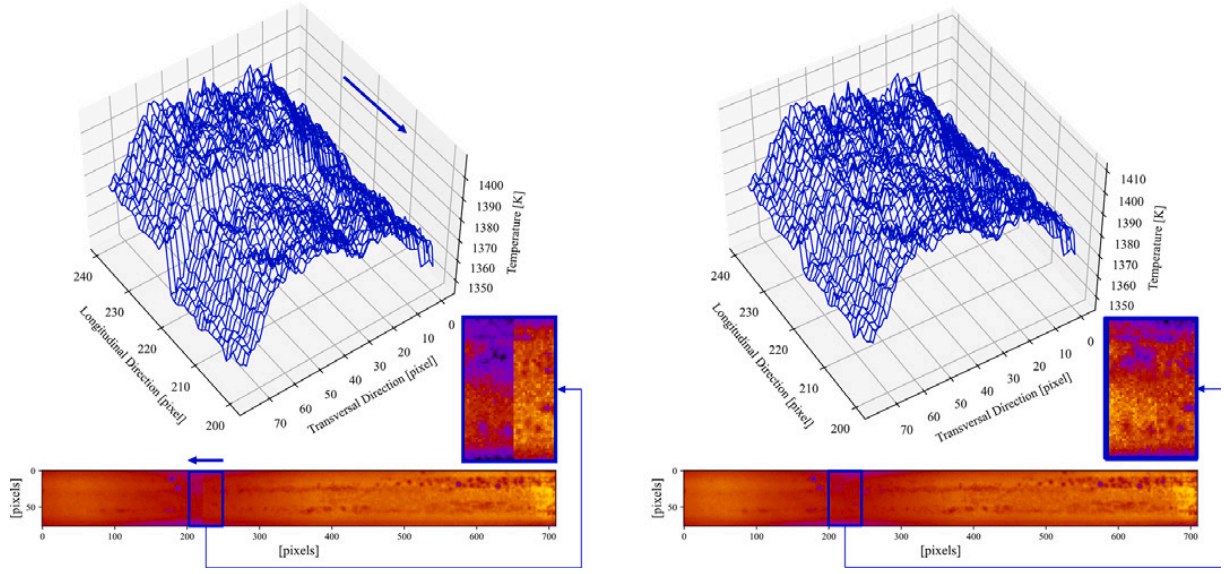


**Fig. 8.** Thermal Image of the bar before (on the left) and after (on the right) the thermal discontinuity correction. The 3D plots represent an enhancement of the discontinuity area. On the left: in the full bar image the colormap represents values from 1292 K (dark blue) to 1484 K (yellow), in the enlargement the colormap goes from 1366 K to 1409 K. On the right: in the full bar image the colormap represents values from 1292 K (dark blue) to 1471 K (yellow), in the enlargement the colormap goes from 1374 K to 1411 K.

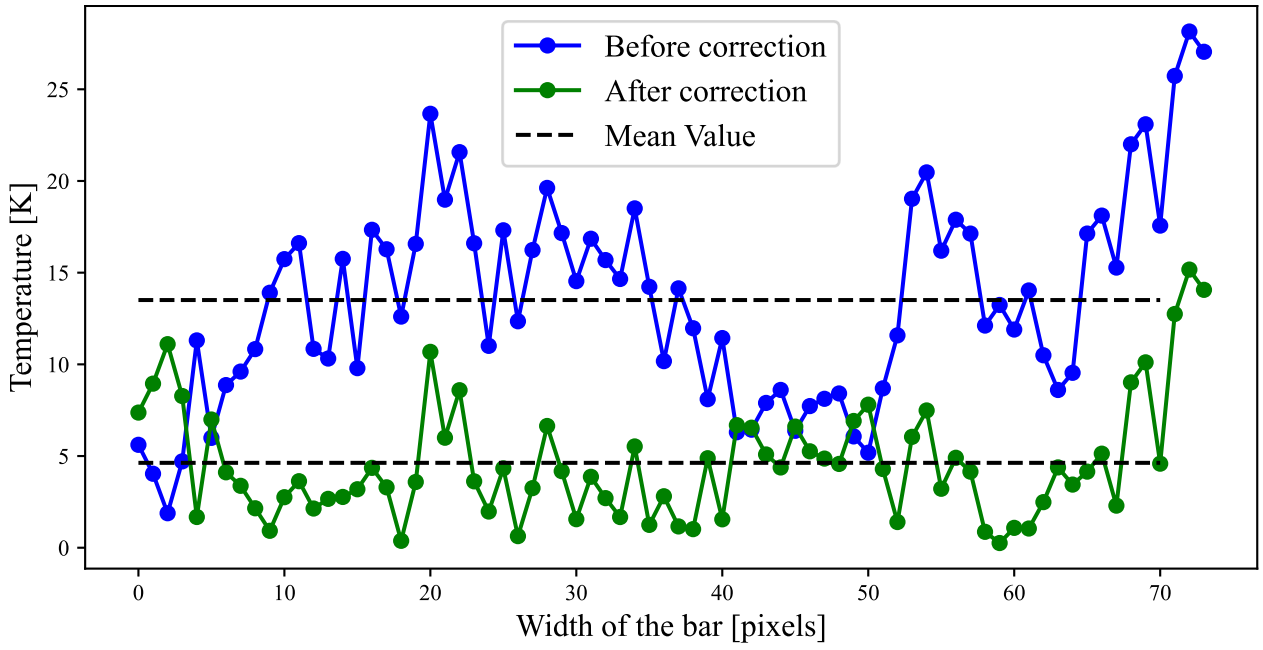


**Fig. 9.** Comparison of temperature differences across the stitching boundary before and after reconstruction.

how many degrees of temperature should be added to each pixel depending on its distance from the exit of the induction furnace.

The same process has been applied to monitor the temperature trend of the tail, selecting three areas on it, and correct temperatures of it (Fig. 12). As previously pointed out, in the first part of the transition the head is still heated by conduction, the tail still being inside the furnace; this fact explains the trend of the temperature profile that undergoes an initial heating and then a cooling phase These curves were also fitted with second-order polynomial functions, with maximum RMSE of 0.65 K and minimum $R^2$ of 0.97.

Fitted curves, one for the head and one for the tail, have been inverted by subtracting the value of the curve at 100 mm of distance from the furnace. Then, the curves have been corrected by applying another constraint: the correction of the tail model in the proximity of the discontinuity summed to the correction of the head model in the proximity of the discontinuity must be equal to the value of the discontinuity ($\Delta T$).

The two modeled correction curves are shown in Fig. 13.

When applied to the two thermal images, this model shows all temperatures at the same distance from the furnace (100 mm) eliminating the discontinuity as shown in Fig. 14.

The correction curves were obtained by modeling the cooling of the material with a second-degree polynomial, the function best suited to the behavior of the product in question. However, should the material properties of the component under inspection or the process parameters (e.g. furnace temperature, or ambient temperature) change, these

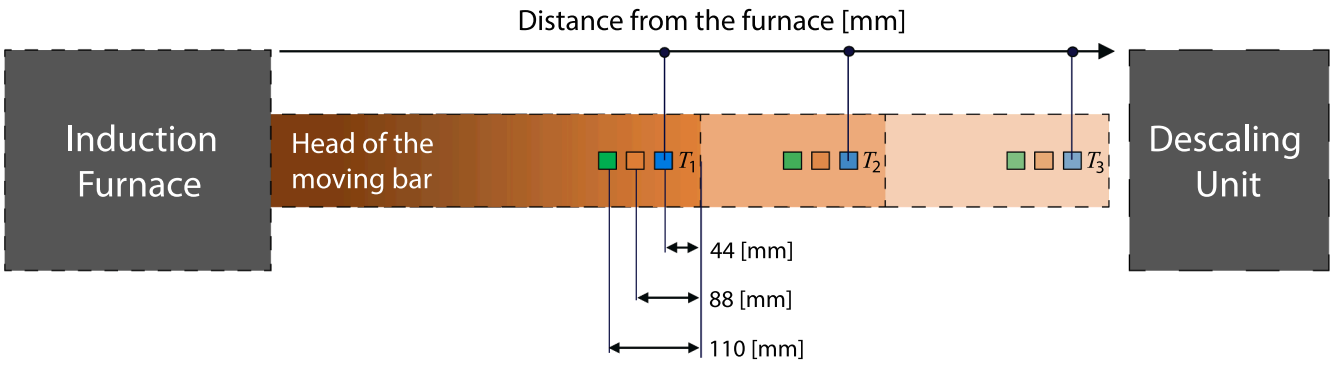


**Fig. 10.** Selected area on the head to monitor the cooling of the bar.

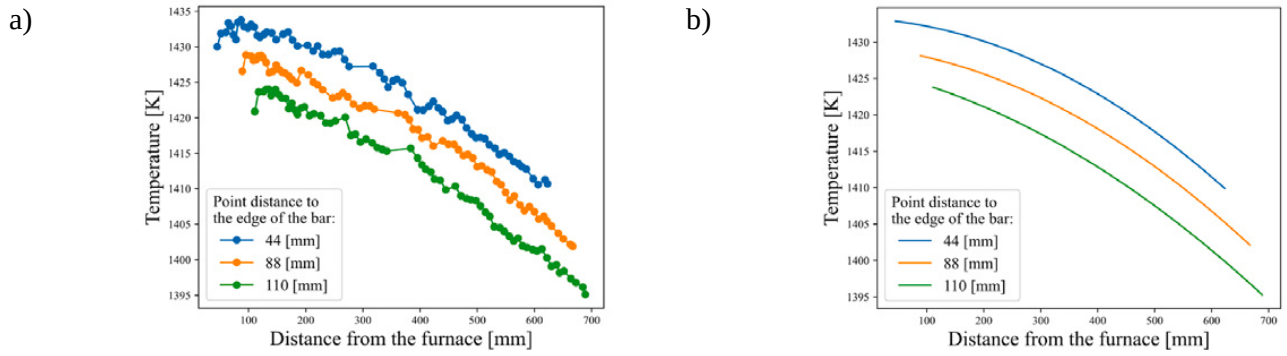


**Fig. 11.** A) temperature trend of three areas of size 5 × 5 mm$^2$ of the bar tail as the distance from the furnace increases. The blue plot refers to an area centered at a point 44 mm away from the edge. The orange plot refers to an area centered at a point 88 mm away from the edge. The green plot refers to an area centered at a point 110 mm away from the edge. b) Polynomial fit of the temperature trends reported in plot a).

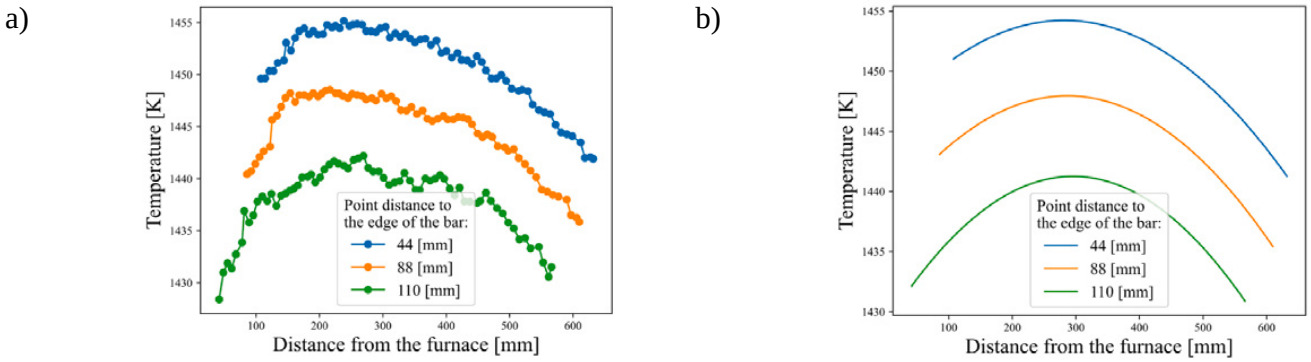


**Fig. 12.** A) temperature trend of three areas of size 5 × 5 mm$^2$ of the bar head as the distance from the furnace increases. The blue plot refers to an area centered at a point 44 mm away from the edge. The orange plot refers to an area centered at a point 88 mm away from the edge of the head of the bar. The green plot refers to an area centered at a point 110 mm away from the edge of the head of the bar. b) Polynomial fit of the temperature trends reported in plot a).

correction curves must be recalculated by performing a video again.

## 4. Application of the reconstruction methods

The first proposed methodology (method n. 1, alignment in time) is highly dependent on specific reconstruction parameters, such as the length of the bar portion available in the tail image, and the *k* parameter (shown in the Fig. 6), which represents the partition of the overlapping area between the tail image and the head image. The reconstruction methodology should be independent of the speed variability, so it is important to assess which parameters are optimal to perform it, and which parameters allow this independence. In particular, the *k* parameter can be chosen during data processing while the amount of available bar in the tail image cannot be changed once the images have been acquired. Therefore, it was also analyzed how *k* could be changed, thus having a *k* that fits the uncertainty on the amount of bar available in the tail image.

Concerning the second methodology (method n. 2, alignment in space), it has been developed such that there is no dependency on these two parameters and therefore no need for a choice of optimal *k*. The accuracy of the methodology does not trend with *k* but depends solely on the uncertainty of the correction model developed. This method has been validated by performing a kind of line-scanning using a video that shows the complete transition of the bar.

### 4.1. Analysis of time-alignment method – method n. 1

First, sources of uncertainty in the first reconstruction methodology

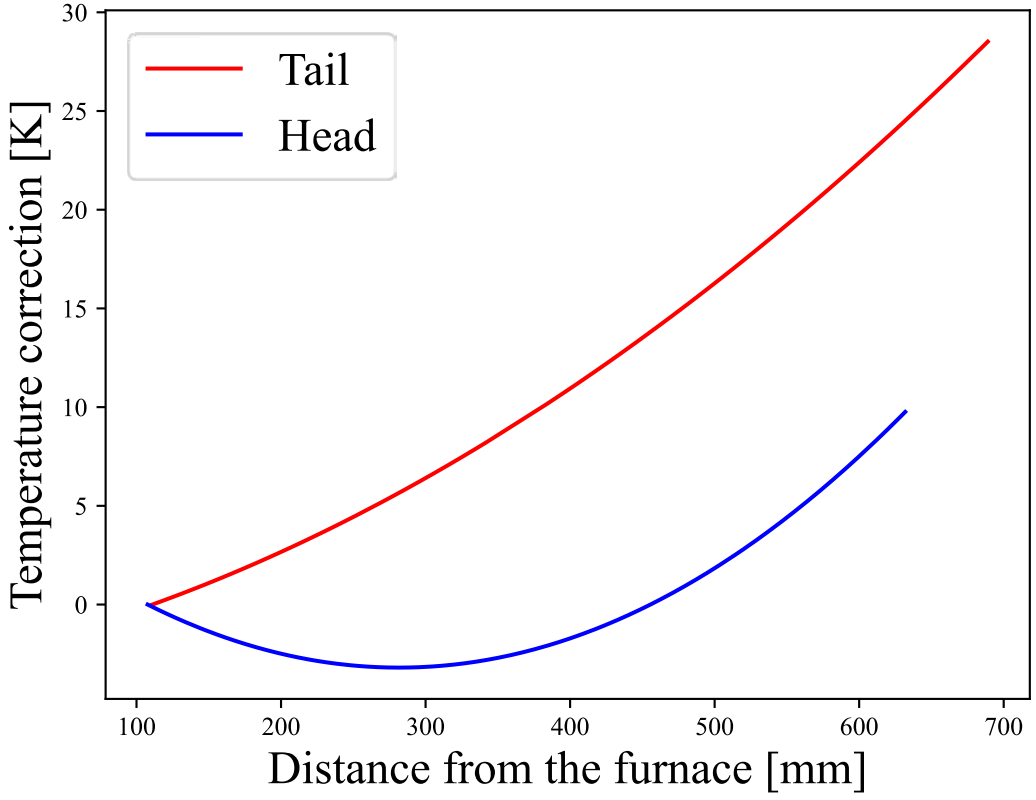


**Fig. 13.** Temperature correction curves of the tail (red) and of the head (blue).

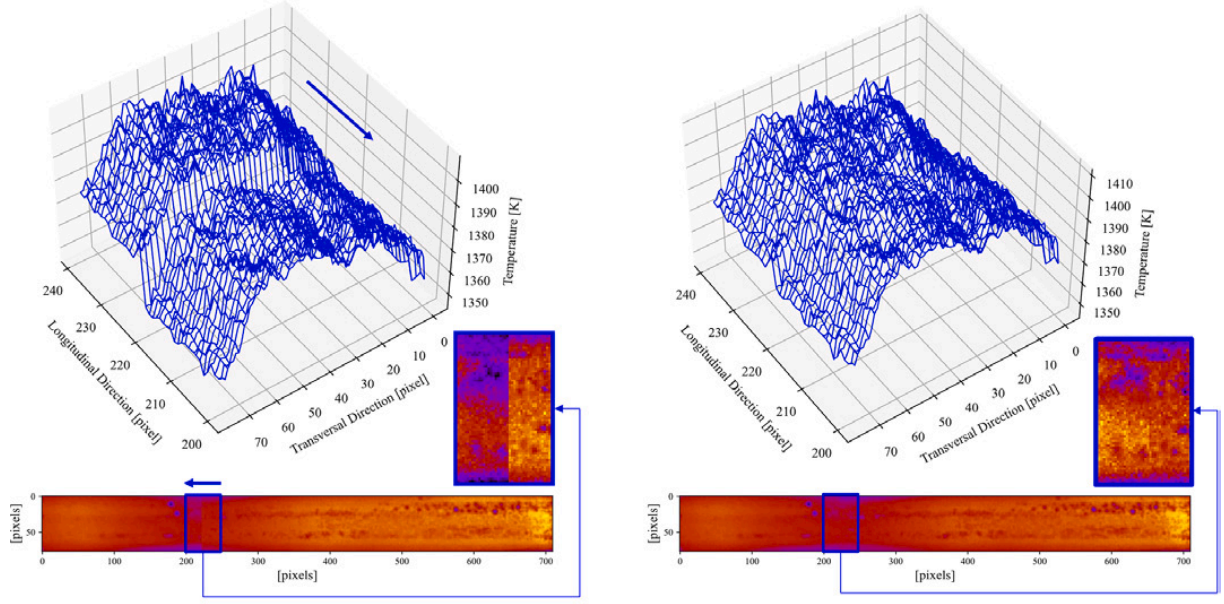


**Fig. 14.** Thermal Image of the bar before (on the left) and after (on the right) the thermal discontinuity correction. The 3D plots represent an enhancement of the discontinuity area. On the left: in the full bar image the colormap represents values from 1292 K (dark blue) to 1484 K (yellow), in the enlargement the colourmap goes from 1366 K to 1409 K. On the right: in the full bar image the colormap represents values from 1303 K (dark blue) to 1493 K (yellow), in the enlargement the colourmap goes from 1374 K to 1411 K.

were assessed. They depend on bar cooling, and consequently on the parameters used for image stitching.

In the following figure (Fig. 15), there are some examples of tail images, all suitable for the geometric reconstruction. In each of these images a different bar-tail length, acquired at different time intervals from the acquisition of the head image, is used. It could also happen, due to the variability of the speed, that at the same acquisition time, different bar-tail lengths are available. Therefore, the authors will refer below to the available bar-tail length.

40 different tail images have been acquired. One might inquire which of these images is optimal for bar reconstruction using method no.1, which involves aligning the tail image temporally with the head

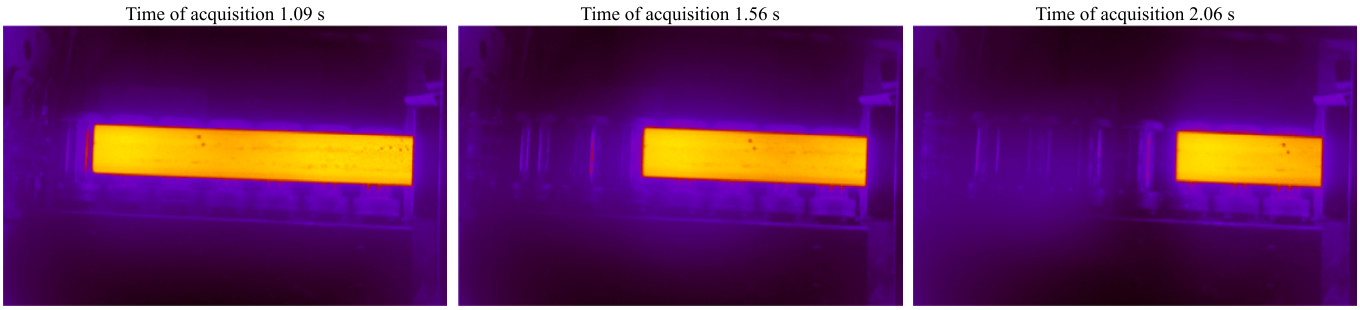


**Fig. 15.** Example of possible tail images. The time of acquisition is expressed as a difference of time from the acquisition of the head image. The thermal maps in the figure represent values in the range 950 to 1448 K (on the left), 913 to 1437 K (on the center), and 889 to 1432 K (on the right).

image. To define which bar-tail length is the best, the average longitudinal profile of the head and the average longitudinal profile of these tails have been correlated in the overlapping window (these profiles are shown in Fig. 16, only 5 profile over the 40 analyzed are shown). As expected, the correlation (Fig. 17) is greater the shorter the time traveled, i.e. the greater the available bar-tail length (at least 400 pixels). The obvious reason for this is that the shorter the length of the tail bar, the more time has elapsed since the exit of the furnace and therefore the more the tail has cooled and the more the temperature difference must be corrected. The correlation is performed using the Pearson coefficient.

The other parameter influencing the reconstruction is the $k$ parameter and it is also crucial: the thermal image of the bar has been reconstructed with the time-alignment methodology using all eligible $k$, each value of $k$ compatible with the size of the overlapping area. In Fig. 18, it is possible to see that the shapes of the average longitudinal profiles are highly dependent on the $k$ parameter. Figure-a shows the variability zone of the average longitudinal profiles. The average longitudinal profiles of the reconstructed bars vary within the shown red interval. Figure-b shows how the value of a point in these profiles varies depending on $k$. It is strongly dependent on the parameter $k$ and

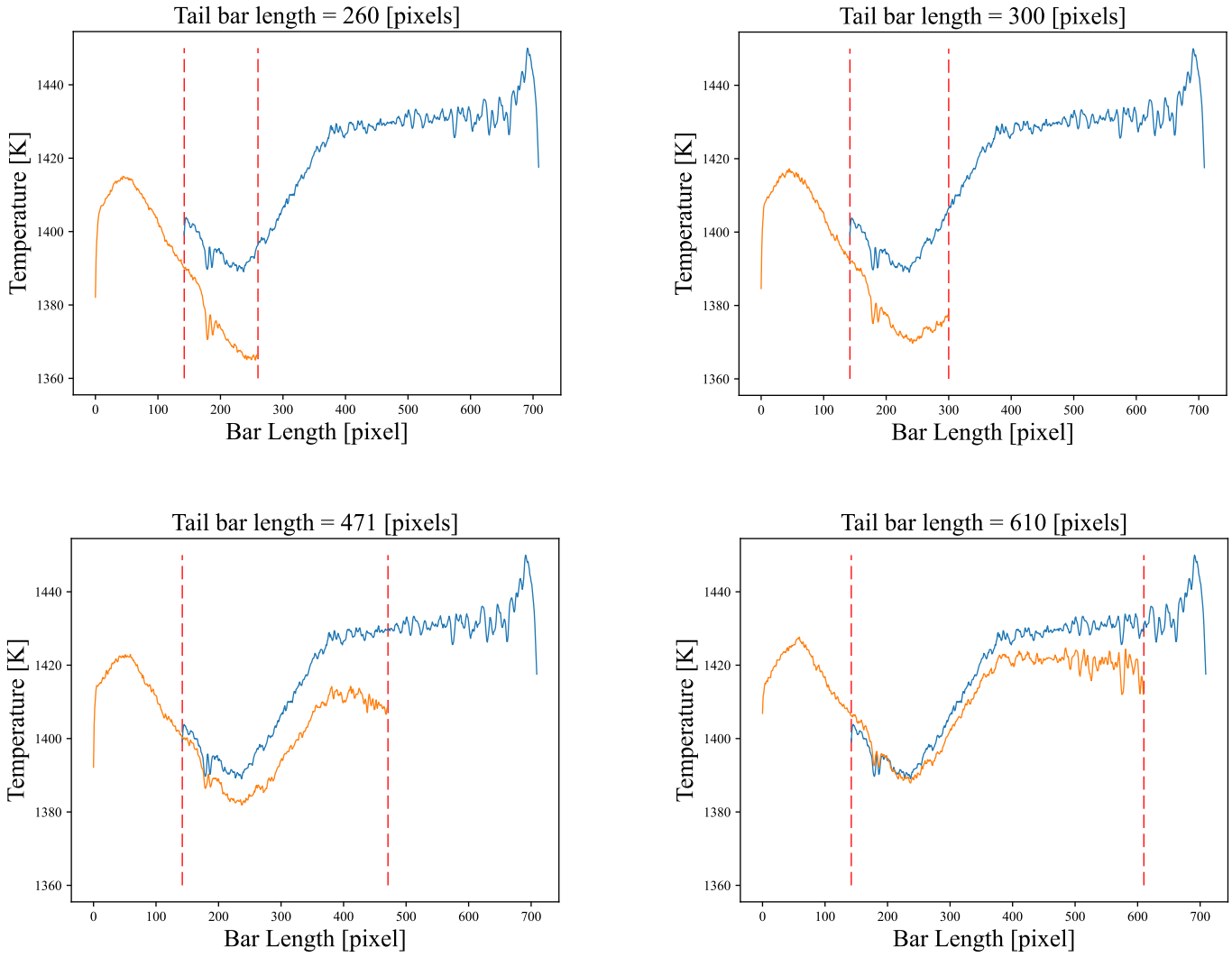


**Fig. 16.** Different longitudinal profiles of the head (blue plots) and tail (orange plot) bars as the portion of the bar available from the tail image decreases.

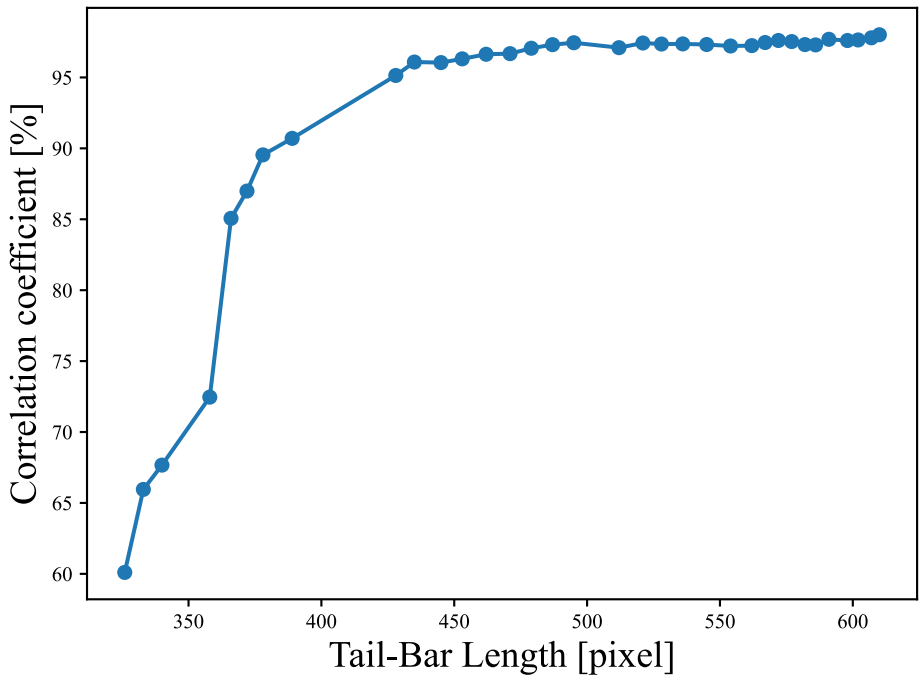


**Fig. 17.** Correlation coefficient between longitudinal profiles in the overlapping area as the amount of bar available in the tail image increases. The longer the tail-bar length, the closer it is to the furnace and the less it has cooled down.

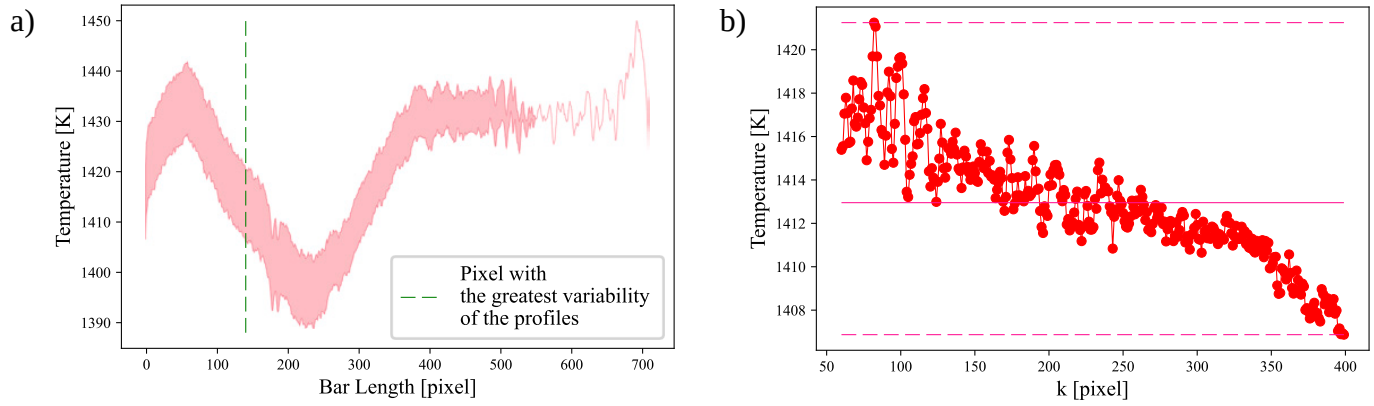


**Fig. 18.** A) interval of variability of alp (average longitudinal profiles); the different profiles were obtained by varying the parameter k. b) temperatures of the same point of each alp as the k parameter changes. the selected point (shown in plot a), green line), is the point of greatest variability.

decrease as it increases.

Looking at the longitudinal profiles (Fig. 19) of the two bars to be joined (tail and head), the tail profile completely changes tendency compared to the head profile, as those points on the tail have already undergone cooling.

Hence, one would need to select a sufficiently large $k$ to mitigate such cooling effects. It can be inferred that the accuracy of the reconstruction using this methodology increases with a greater availability of tail-bar length and higher parameter $k$, within the acceptable range of $k$ values.

As announced, $k$ can be managed, being a parameter of the reconstruction algorithm. However, the length of the tail image is not completely under control. An adaptive $k$ can be used, and the best $k$ can be selected depending on how far the bar has travelled out of the furnace. In the 3D graph below (Fig. 20), it is possible to see how the reconstructed bar temperatures vary as the available tail length and parameter $k$ change. Specifically on the z-axis is the mean temperature calculated on the reconstructed bar for each combination of bar-tail length and $k$, which is one of the possible indicators. One could also use the variability of the average temperature of the reconstructed bar. The values of the longitudinal profiles best ensure the consistency of the shape of the distribution.

The desired temperature value is known, having previously analyzed the suitable parameters in x and y, i.e. those for which you have as much tail bar as possible available and k as large as possible. Then it is possible to build an $xy$-plane at that desired temperature, and the intersection (Fig. 20-a blue points) of the graph with the plane gives the parameters locus that allow the right reconstruction, i.e., the length-tail and $k$ pairs to perform the reconstruction always in the same way. These intersection points can be fitted with a straight line whose equation is shown in the Fig. 21. The linear regression fits the data with a linear correlation coefficient $R^2 = 0.97$. A curve was obtained that defines, for each available tail length, which value of the parameter $k$ allows to obtain the optimal reconstruction.

### 4.2. *Validation of space-alignment method*

Concerning the second methodology, which uses the model to align the pixel in the space (at 100 mm distance from the exit of the furnace),

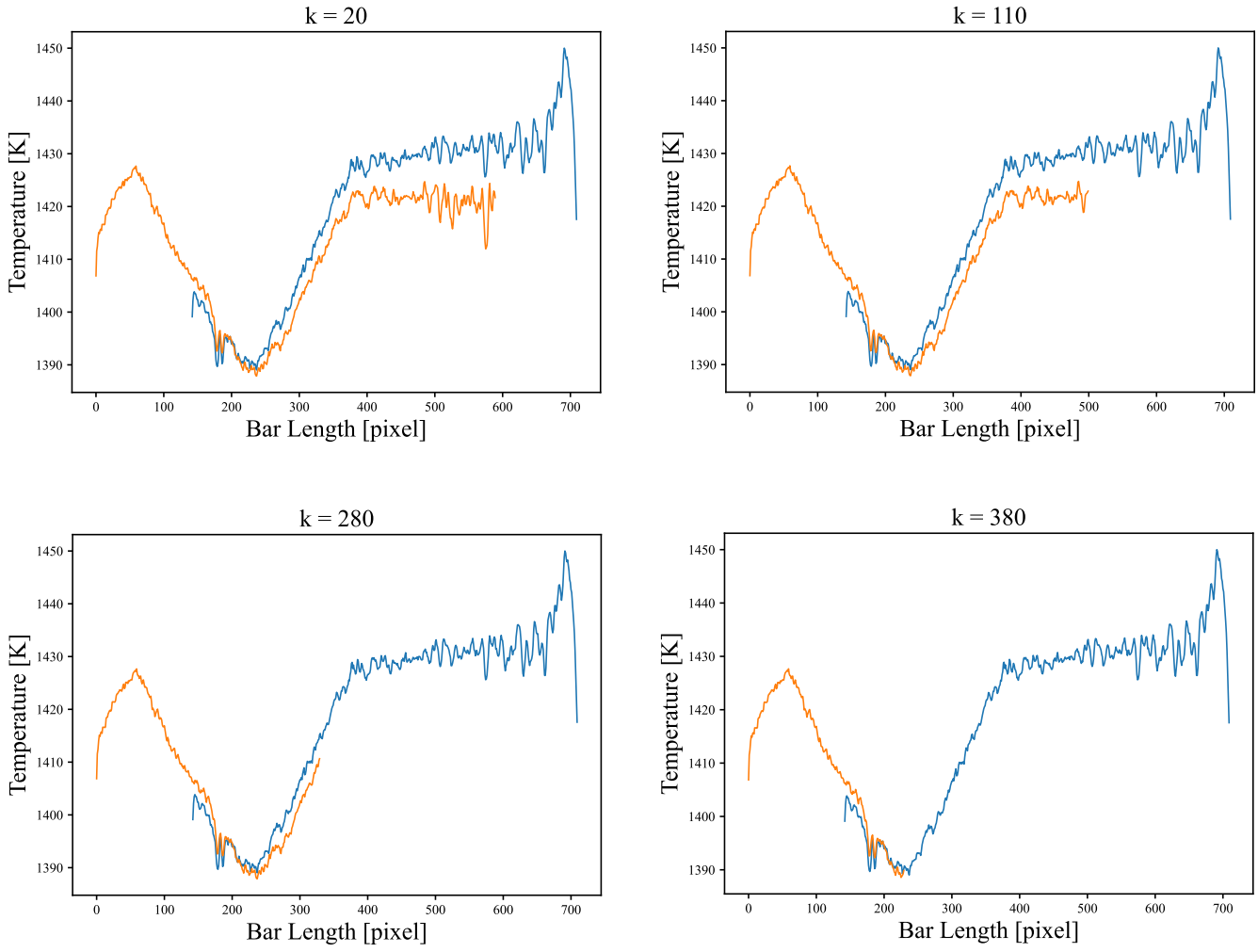


**Fig. 19.** The orange curves are the average longitudinal profiles of the tail images with k-parameter increase.

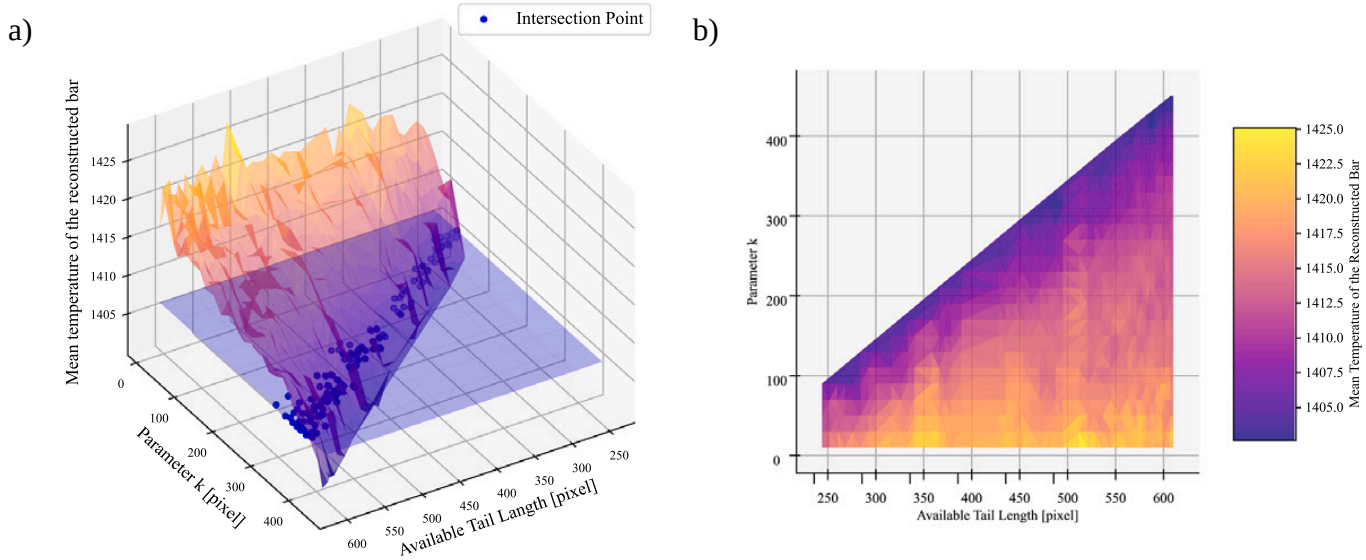


**Fig. 20.** A) 3d plot showing the relationship between temperatures of the reconstructed bars and the length of the bar-tail and the k-parameter. b) top view of the 3d graph. the third dimension (temperature) is represented as a false-color image.

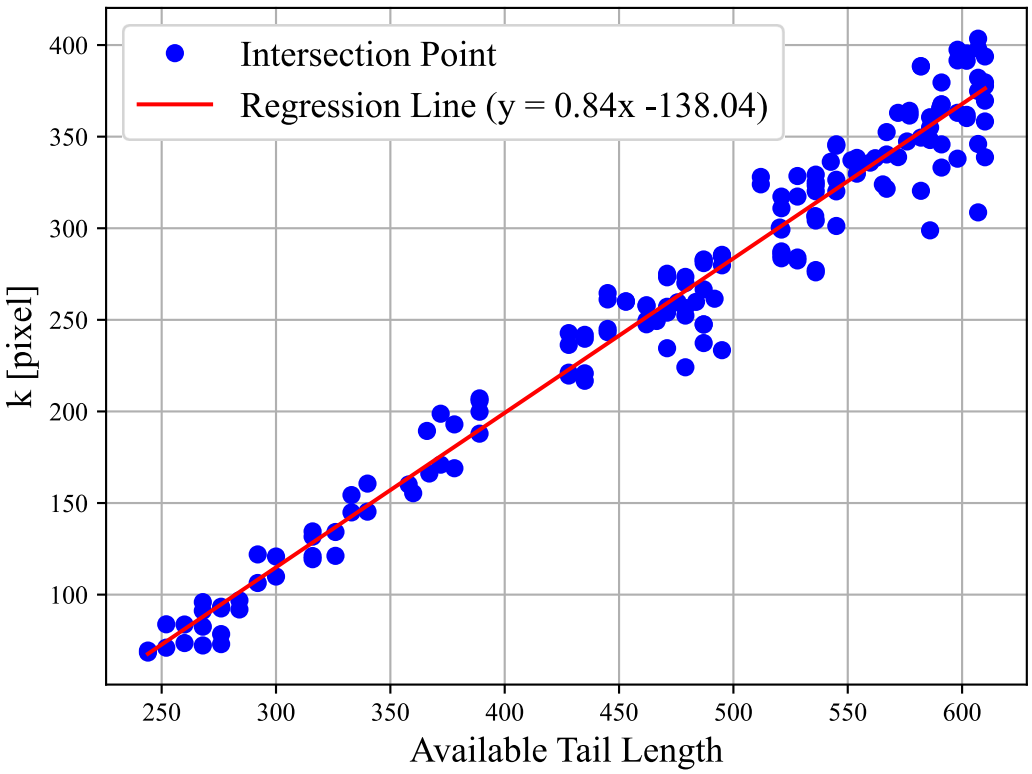


**Fig. 21.** Relationship between parameter k and the tail length to get the optimal combination of parameters to use for the reconstruction method n.1.

as previously mentioned, it is not dependent on the reconstruction parameters. Focus will be on its validation.

To validate the reconstruction method, the authors performed a kind of line-scanning on a video that shows the complete transition of the bar from the induction furnace to the descaling unit. The value of each point of the bar passing in this position has been recorded. This monitored position is shown in Fig. 22 (yellow line).

The average longitudinal profile of the bar has been reconstructed using line-scanning and compared with the average longitudinal profile of the bar after reconstruction with the second developed methodology. The two profiles are plotted together in Fig. 23 with separate abscissa axes, and different scales on bar length dimension. The mean

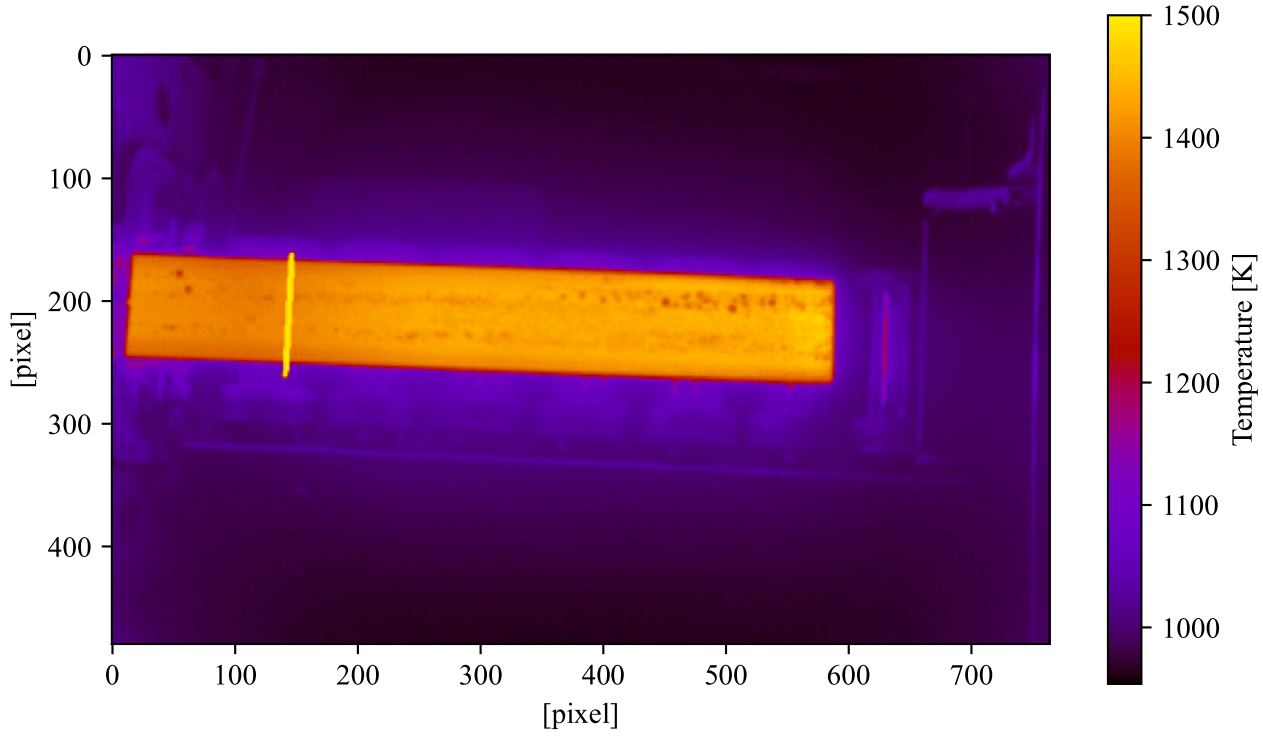


**Fig. 22.** Position of the monitored line (yellow line) on the video to perform line-scanning.

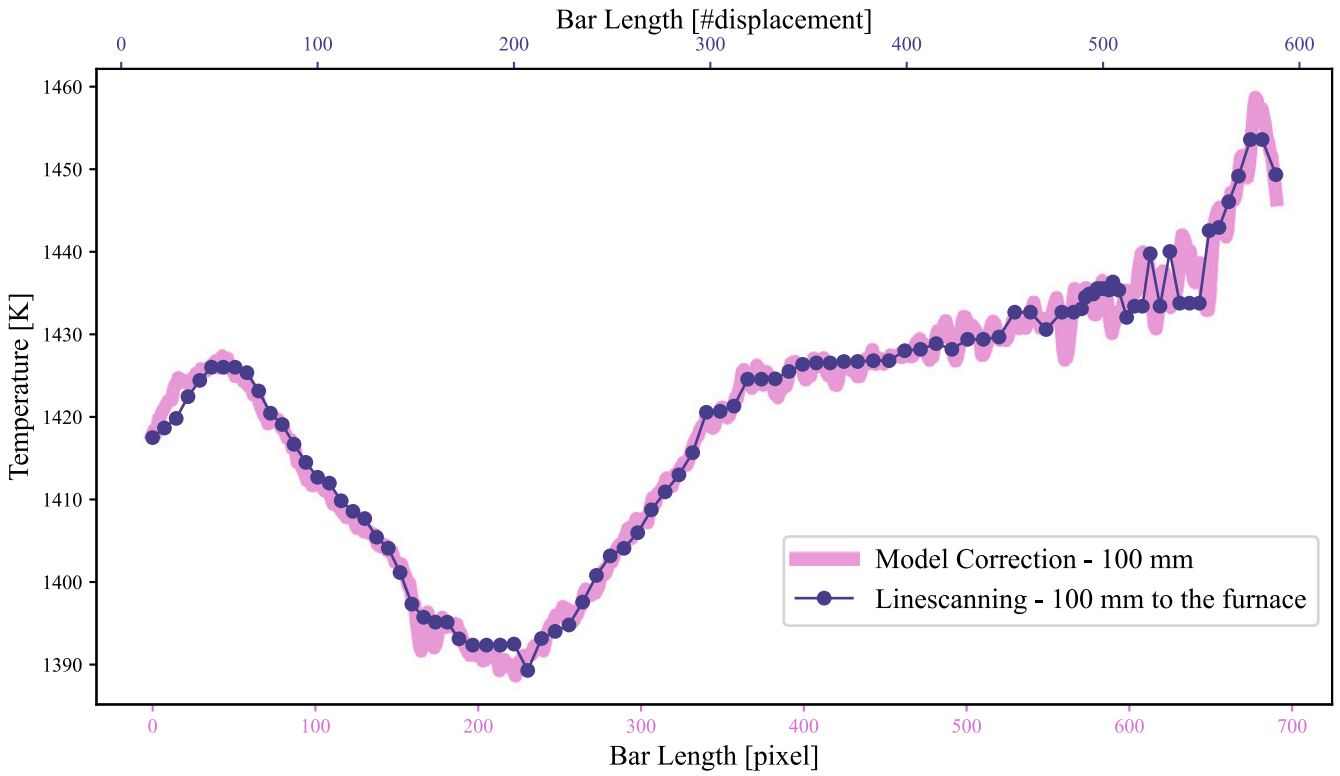


**Fig. 23.** Comparison of average longitudinal profile of the reconstructed bar using method No.2 correction (pink) and the same profile from the image acquired using line-scanning (dark blue).

longitudinal profile of the image reconstructed using the second methodology has as its abscissa the number of pixels of the bar length. The line-scanning profile has as its abscissa the bar displacement, calculated for this specific bar. The comparison is shown in Fig. 23: the two profiles are well correlated and match each other. The profile with the largest number of samples was subsampled to quantify the linear correlation between the two profiles, resulting in an $R^2$ of 0.97. This linear correlation is shown in the Fig. 24.

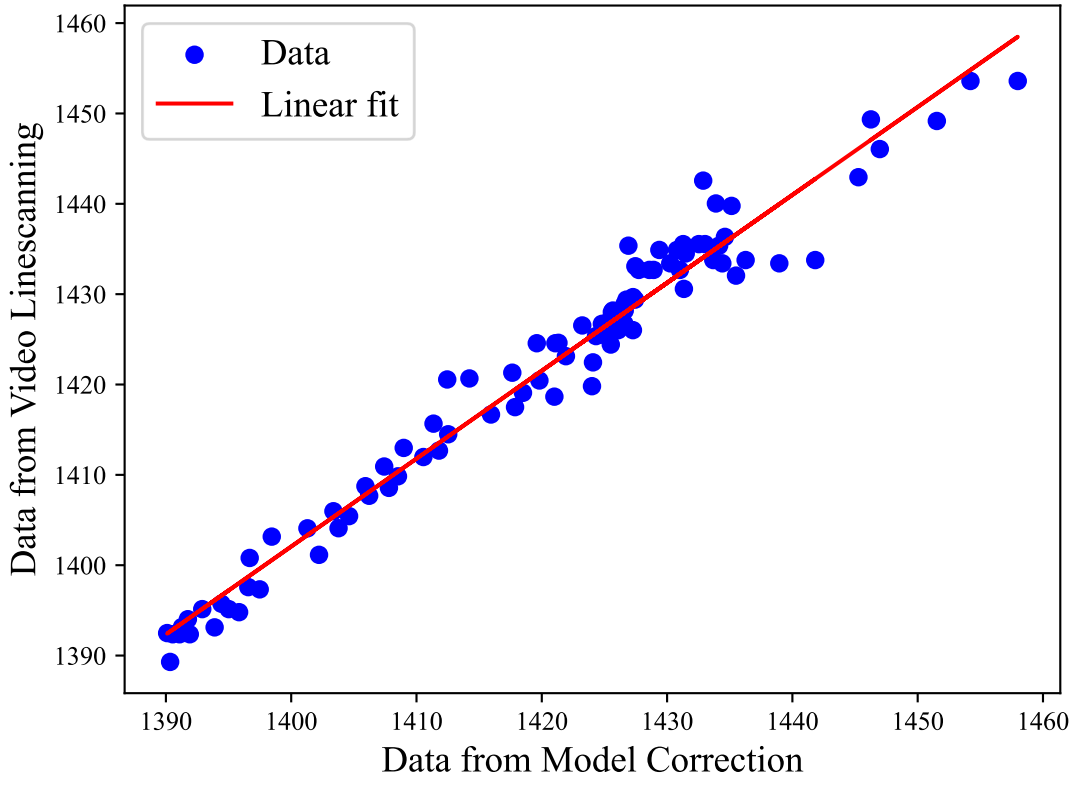


**Fig. 24.** Linear correlation between the average longitudinal profile of the reconstructed bar using method no.2 and the one acquired using video line-scanning.

### 4.3. Uncertainty analysis

The methodologies presented in Section 3 are applied to reconstruct the thermal distribution of products. Product features are extracted from it, such as the mean temperature of the bar or the percentage area covered by oxides on the bar surface. The reconstruction process influences these parameters leading to uncertainty. The uncertainty of the average bar temperature and the uncertainty in the estimation of anomaly (oxides area) size.

To evaluate the uncertainty associated with the parameters derived from the bar surface thermal distribution, potential sources of error must be analyzed.

Concerning the estimation of the average bar temperature, its uncertainty is associated with the parameters of geometric stitching, specifically the available tail length and the parameter k (analyzed in Section 4.1). The average temperature of the bar was measured as these parameters were varied, allowing an evaluation of how changes in tail length and k affect the bar's temperature.

The uncertainty associated with the anomaly size identification is correlated to the pixel length used for geometrical stitching. The resolution of the thermal image is limited, and the edges of the bar appear not-sharp. Suppose there are such uncertainties in the bar crop and thus in the geometric stitching, and anomalies are present in the overlapping area. In that case, likely, the dimensions of the anomaly are incorrectly measured. To show this effect, the length of the bar is varied so that the stitching point is shifted by $\pm$ 15 pixels relative to the optimum point. The change in size of the anomaly is then measured.

This approach enables a clearer understanding of how stitching parameters impact results in terms of temperature and anomaly dimensions.

#### 4.3.1. Influence of the tail-bar length and k parameter

Ten different tail images have been acquired, one with the optimal bar-tail length and the others with shorter lengths. After the geometric stitching, performed by knowing the bar length and pixel-mm ratio, both correction methodologies have been applied to eliminate the discontinuities resulting from the matching and reconstruct the thermal image of the bar.

In the application of method no.1, an adaptive $k$ parameter was used, in accordance with the above. In this way, compared to the case where an equal $k$ is used for all bars, the temperature of the reconstructed bar is less dependent on the available tail length and consequently on the time of acquisition. Always using the same value of $k$, the mean temperature of the reconstructed bars has been monitored and its dispersion has been calculated. The dispersion of the mean temperature has been calculated as the difference between the maximum and minimum obtainable mean temperature values. It turned out that, when using different tail images without changing $k$, the temperature could vary by 6 K. In contrast, if $k$ were varied in accordance with the selected tail image, the dispersion of mean temperature values would be reduced to 1 K.

The average longitudinal profiles of four bars reconstructed using the first methodology are shown in Fig. 25. The discontinuity is not present, and the resulting distribution is no longer dependent on the chosen parameters.

To reconstruct with the second methodology, an equal $k$ was set for all bars, and it can be seen from the reconstructed profiles that this method is not dependent on the $k$ parameter and how much cooling the tail has undergone. The dispersion of these mean temperatures is 1 K, without changing $k$.

#### 4.3.2. Presence of anomalies in the overalapping area

If anomalies are present near the discontinuity, errors in geometric reconstruction can lead to an underestimation or overestimation of the anomaly size. If the anomaly is substantial, these errors can also prevent the discontinuity from being fully corrected.

Consider the two images (head and tail) shown in Fig. 26. An artificial anomaly simulating the presence of oxide of 81 pixels area, with an apparent temperature of approximately 1300 K, was introduced near the point where the two bar segments will be joined. The two images are aligned through both geometric and thermal stitching processes. The geometric stitching carries uncertainty associated with the input parameters (such as tail length, the parameter k, and the desired length in pixels) described in Fig. 6. A head-to-tail mismatch is simulated by varying the bar's target length within a range of $-10$ to $+10$ pixels from the optimal length. This adjustment allows to observe the impact of these variations on the alignment accuracy and the resulting dimensions of the anomaly.

The reconstructed image using the correct parameters is shown in Fig. 27. In Fig. 27-a, the geometrically stitched image is displayed, followed by images corrected with both methods. Fig. 27-b presents close-ups of the stitching area, showing three different configurations: one where the match is exact, allowing for accurate detection of the oxide; another where the oxide size is underestimated; and a third where it is overestimated.

To assess the uncertainty of the geometric reconstruction method, the variation in oxide size and the average bar temperature was evaluated by adjusting the input length in pixels provided to the algorithm. The oxide size fluctuated between 55 and 136 pixels, as shown in Fig. 28, corresponding to an area range of 78 to 193 mm$^2$. Therefore, the uncertainty is equal to 57.5 mm$^2$, a half of the range.

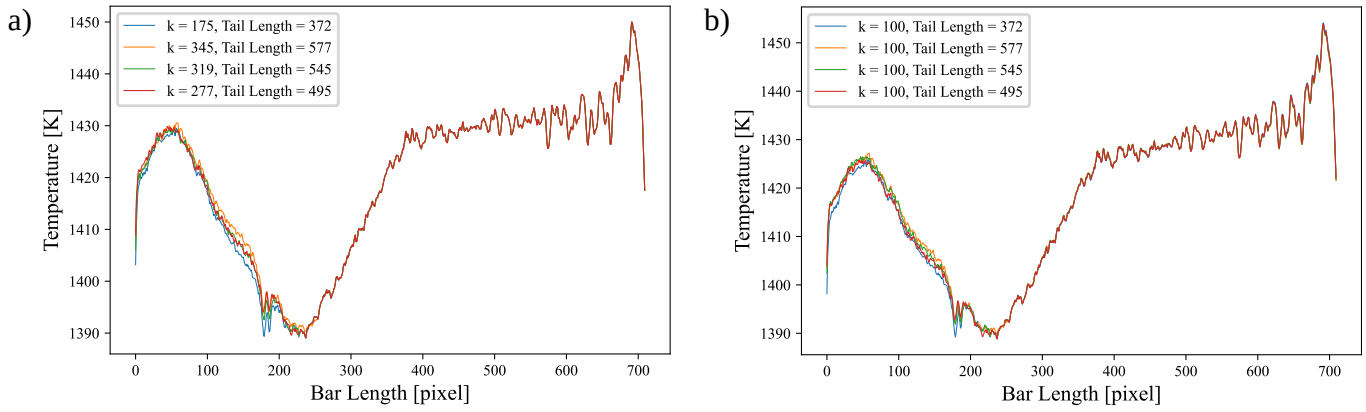


**Fig. 25.** Average Longitudinal Profile of the reconstructed bar using four different tail images. a) Method No.1 – Time-alignment: adding the $\Delta$ T of the discontinuity to the whole tail image using an adaptive k parameter depending on the available length of tail bar. b) Method No.2 – Space-alignment: using cooling correction curve to simulate line-scanning and always using the same k parameter.


**Fig. 26.** A) tail, and b) head of the bar including an artificial anomaly in the overlapping area. the color map represents value from 1298 to 1473 K (on the left) and from 1300 K to 1510 K (on the right).

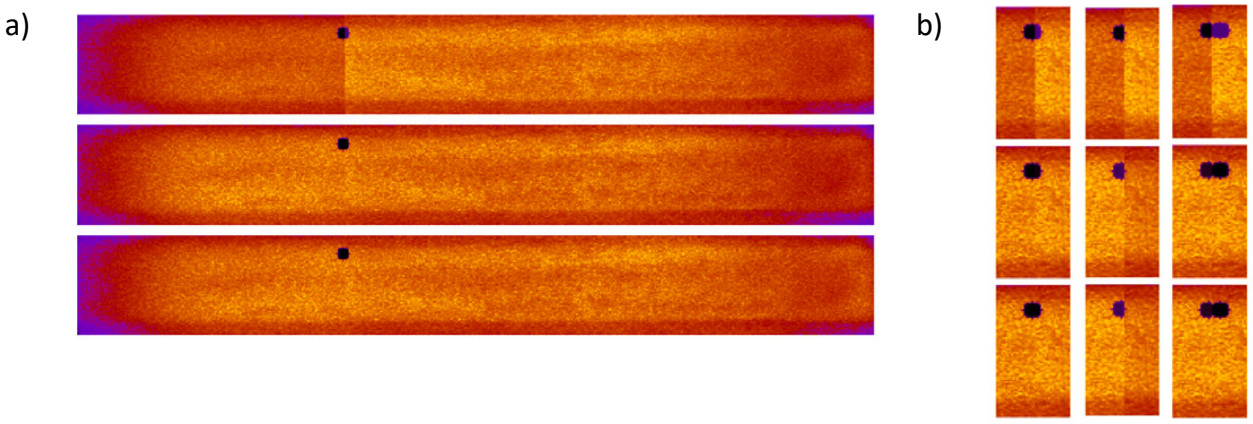


**Fig. 27.** Image with an artificial anomaly in the overlapping area. (a) Stitching using the correct length value. At the top, the image after geometric stitching; in the middle, after applying Method n.1; and at the bottom, Method n.2. (b) Zoomed-in view of the stitching area showing the optimal case, a case where part of the anomaly is lost, and a case where it appears twice.

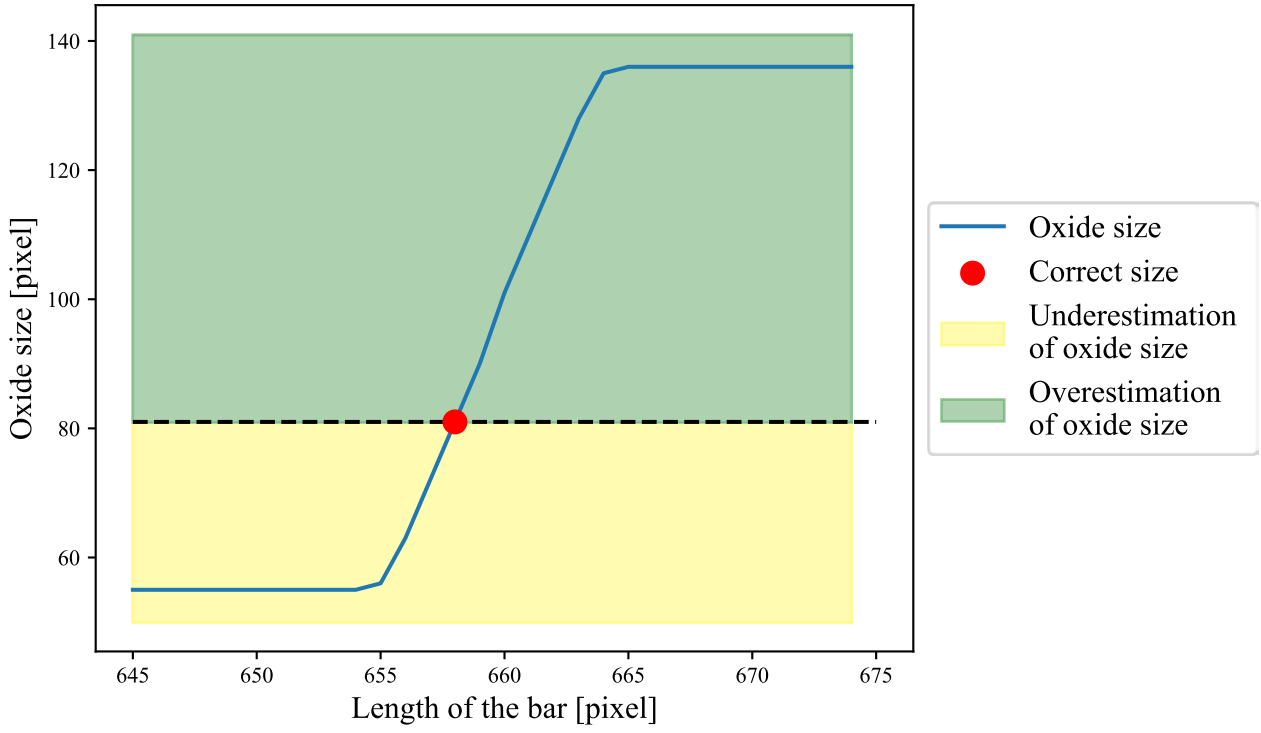


**Fig. 28.** Variation of oxide size with the input desired length.

### 4.4. *Example of application*

Both methodologies have been tested on a set of 100 products, some of which exhibited partial oxidation. Two products are presented in Fig. 29 as example. The oxides present in these products typically do not display significant intensity compared to those created artificially. As a result, the discontinuity is consistently eliminated successfully, since this value does not affect the average profile used for reconstruction.

For each bar, the area covered by oxides is calculated, and based on the analyses conducted, the detected oxides have an associated uncertainty of 57.5 $mm^2$, a half of the variability range calculated above.

Since a k dependent on the length of the available tail was used, the uncertainty on the average bar temperature is ±1K.

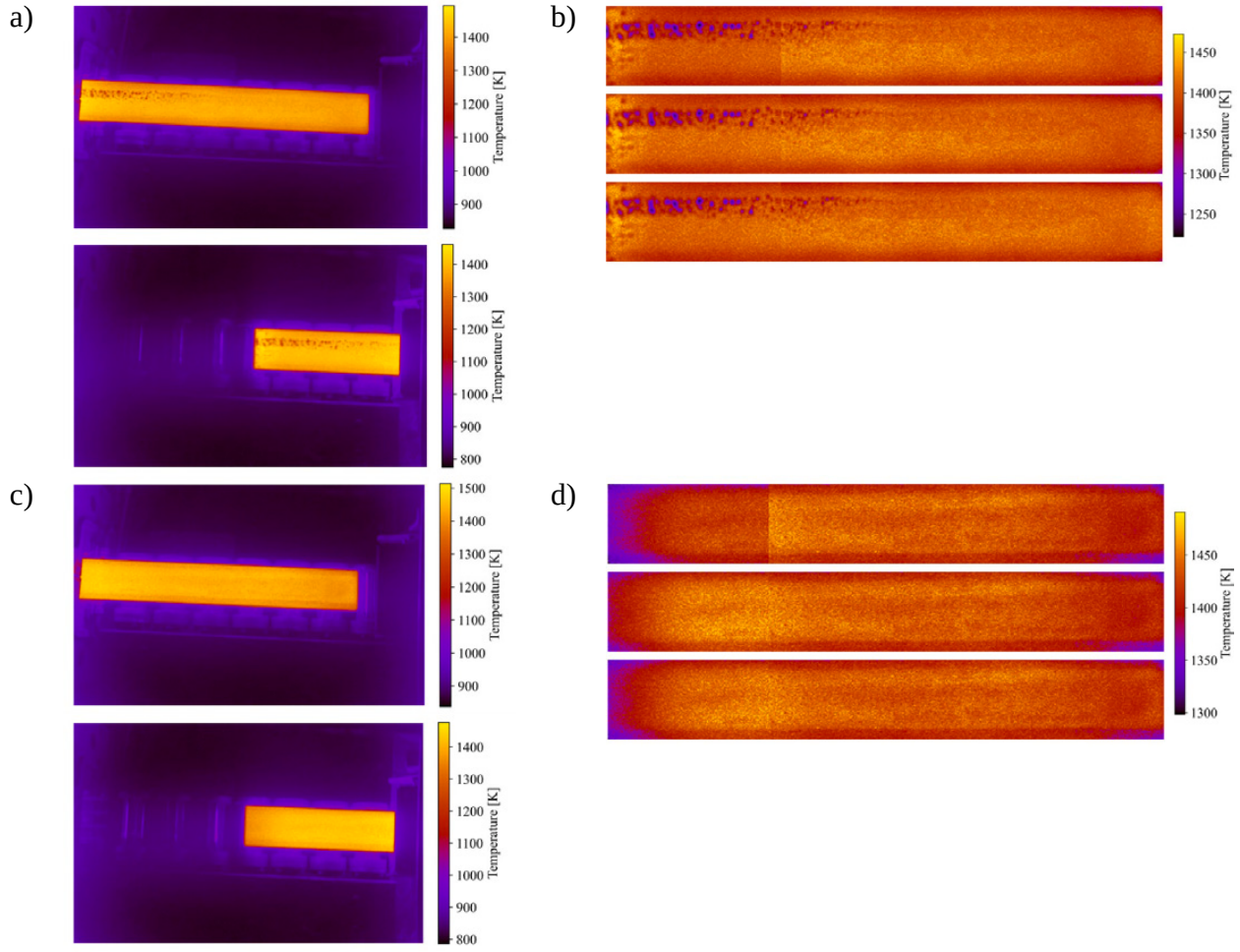


**Fig. 29.** Examples of bars on which the two methodologies were applied. a) and c) show the original head and tail images. b) and d) show the respective images stitched geometrically (top image), then thermally corrected first with Method n.1 (central image) and then Method n.2 (bottom image).

## 5. Conclusions

In the installation of thermal cameras in real manufacturing contexts, imaging moving objects like steel bars, there may be a condition in which not the whole object can be framed. The authors have described an industrial use case in which thermal images of steel bars at very high temperatures, in motion at an unsteady speed and undergoing a thermal transient must be acquired. The thermal camera cannot frame the entire bar, therefore two images are acquired in sequence; of course, each image is acquired at a different time, while the bar is cooling. The images must be combined into a single information field to improve the efficiency of the data pipeline. Therefore, the images must be merged to reconstruct the thermal image of the bar and obtain useful information on the symmetry of the temperature distribution of the object. In the literature, there is a gap in thermal image stitching match solutions at very high temperatures of objects in motion, where thermal corrections are necessary to eliminate discontinuities caused by the cooling of the bar during its transition. This is a problem in which temperature T varies in space *x-y* and time *t*.

Two methods are presented for correcting the thermal data and eliminating the spatial discontinuity appearing when stitching the two images without any correction. The two methods have two different objectives: to align the temperature data of the two images in time (as if a single snapshot framing all the bar was taken) or to align the temperature data of the two images in space (as if line-scanning was done). The first methodology is easier to apply but it is more dependent on acquisition and reconstruction parameters, such as the time the bar has passed completely out of the furnace, which corresponds to the amount of bar available in the tail image, and the partition of overlap area between head and tail image (named k parameter). An analysis was performed that led to the optimal choice of these parameters to minimize the variability of the temperature distribution as the acquisition parameters changed. An adaptive *k*, dependent on the available tail length of the bar in the tail image, helps in reducing the uncertainty of the mean temperature of the reconstructed bar from 6 K to 1 K. The second methodology does not depend on these acquisition parameters, it has the same performance as the other methodology regardless of these parameters, but it requires a bar cooling model that can be difficult to achieve being phenomena with so many heat transfer sources. In addition, an analysis of the main sources of uncertainty affecting the results of the proposed methods was carried out. It was demonstrated that these methods are applicable and reliable in a real industrial production context, allowing for accurate thermal reconstruction of the bar and precise evaluation of parameters such as mean temperature and area covered by oxides. This approach ensures that uncertainties arising from the geometric stitching process and image resolution do not compromise the reliability of the information obtained for condition monitoring.

## CRediT authorship contribution statement

**Vittoria Medici:** Writing – review & editing, Writing – original draft, Visualization, Validation, Software, Methodology, Investigation, Formal analysis, Data curation, Conceptualization. **Milena Martarelli:** Formal analysis, Investigation, Methodology, Project administration,

Supervision, Validation, Writing – review & editing. **Paolo Castellini:** Methodology, Investigation, Formal analysis, Conceptualization. **Helmert Van De Kamp:** Software, Investigation, Data curation, Conceptualization. **Nicola Paone:** Writing – review & editing, Supervision, Resources, Project administration, Methodology, Investigation, Funding acquisition, Formal analysis, Conceptualization.

## Declaration of competing interest

The authors declare that they have no known competing financial interests or personal relationships that could have appeared to influence the work reported in this paper.

## Acknowledgment

This work was partially supported by the OPENZDM project. This is a project from the European Union's Horizon Europe research and innovation program under Grant Agreement No. 101058673 in the call HORIZON-CL4-2021-TWIN-TRANSITION-01.

## Data availability

Data will be made available on request.

## References

[1] F. Psarommatis, G. May, P.-A. Dreyfus, D. Kiritsis, Zero defect manufacturing: state-of-the-art review, shortcomings and future directions in research, *Int. J. Prod. Res.* 58 (1) (2020) 1–17, https://doi.org/10.1080/00207543.2019.1605228.

[2] V. Medici *et al.*, "Integration of Non-Destructive Inspection (NDI) systems for Zero-Defect Manufacturing in the Industry 4.0 era," in *2023 IEEE International Workshop on Metrology for Industry 4.0 & IoT (MetroInd4.0&IoT)*, Brescia, Italy: IEEE, Jun. 2023, pp. 439–444. doi: 10.1109/MetroInd4.0IoT57462.2023.10180016.

[3] M. Vidoni, A. Mendel, G. Hirt, Profile strip casting with inline hot rolling: numerical simulations for the process chain design, *Key Eng. Mater.* 611–612 (May 2014) 1568–1575, https://doi.org/10.4028/www.scientific.net/KEM.611-612.1568.

[4] J. Jones, Enhancing the accuracy of advanced high temperature mechanical testing through thermography, *Appl. Sci.* 8 (3) (2018) 380, https://doi.org/10.3390/app8030380.

[5] M. Sisti, C. Falsetti, P.F. Beard, Infrared temperature measurements on fast moving targets: a novel calibration approach, *Measurement* 225 (2024) 113870, https://doi.org/10.1016/j.measurement.2023.113870.

[6] F. Schausberger, K. Speicher, A. Steinboeck, M. Jochum, A. Kugi, Two illustrative examples to show the potential of thermography for process monitoring and control in hot rolling, *IFAC-Pap.* 48 (17) (2015) 48–53, https://doi.org/10.1016/j.ifacol.2015.10.076.

[7] G. R. Peacock, "Review of noncontact process temperature measurements in steel manufacturing," presented at the AeroSense '99, D. H. LeMieux and J. R. Snell, Jr., Eds., Orlando, FL, Mar. 1999, pp. 171–189. doi: 10.1117/12.342284.

[8] M. Viale, O. Martin, F. Muratori, U. Bertezzolo, J. Perez, and J. Usart, "Application of on-line infrared thermography in steel making industry," presented at the Defense and Security Symposium, Orlando, Florida, USA, Apr. 2007, p. 65410H. doi: 10.1117/12.721225.

[9] S. Koch J. Schroeder, "In-Line Inspection of Hot-Rolled Steel Billets by Heat Flux Thermography," in *Proceedings of the 2012* International *Conference on Quantitative InfraRed Thermography*, QIRT Council, 2012. doi: 10.21611/qirt.2012.102.

[10] T. Husmann, C.S. Magnus, Thermography in incremental forming processes at elevated temperatures, *Measurement* 77 (2016) 16–28, https://doi.org/10.1016/j.measurement.2015.09.004.

[11] M. He, L. Zhang, W. Zheng, Y. Feng, Crack detection based on a moving mode of eddy current thermography method, *Measurement* 109 (Oct. 2017) 119–129, https://doi.org/10.1016/j.measurement.2017.05.041.

[12] E. A. Semenishchev, V. V. Voronin, A. A. Zelensky, A. Alepko, S. S. Agaian, "Improving the accuracy of combining pairs of thermal images based on the analysis of visual information," in *Electro-Optical and Infrared Systems: Technology and Applications XVIII and Electro-Optical Remote Sensing XV*, D. L. Hickman, H. Bürsing, G. W. Kamerman, and O. Steinvall, Eds., Online Only, Spain: SPIE, Sep. 2021, p. 12. doi: 10.1117/12.2600585.

[13] B. Deng, et al., Line scanning thermography reconstruction algorithm for defects inspection with novel velocity estimation and image registration, *IEEE Sens. J.* 21 (10) (May 2021) 11555–11568, https://doi.org/10.1109/JSEN.2020.3034460.

[14] N. Puthiyaveettil, K. Renil Thomas, P. Myrach, M. Ziegler, P. Rajagopal, K. Balasubramaniam, "Defect detection in steel bars up to 600 °C using laser line thermography", *Infrared Phys. Technol.* 111 (Dec. 2020) 103565 https://doi.org/10.1016/j.infrared.2020.103565.

[15] H. Zhang, P. Verberne, S.A. Meguid, C. Ibarra-Castanedo, X.P.V. Maldague, Autonomous high resolution inspection of kiss-bonds skins of carbon nanotube reinforced nanocomposites using novel dynamic line-scan thermography approach, *Compos. Sci. Technol.* 192 (2020) 108111, https://doi.org/10.1016/j.compscitech.2020.108111.

[16] E.A. Moyseychik, V.P. Vavilov, M.V. Kuimova, Infrared thermographic assessment of heat release phenomena in steel parts subjected to quasi-static deformation, *Measurement* 185 (2021) 110117, https://doi.org/10.1016/j.measurement.2021.110117.

[17] Z. Wang, Z. Yang, Review on image-stitching techniques, *Multimed. Syst.* 26 (4) (2020) 413–430, https://doi.org/10.1007/s00530-020-00651-y.

[18] M. Brown, D.G. Lowe, Automatic panoramic image stitching using invariant features, *Int. J. Comput. Vis.* 74 (1) (2007) 59–73, https://doi.org/10.1007/s11263-006-0002-3.

[19] E. Adel, M. Elmogy, H. Elbakry, "Real time image mosaicing system based on feature extraction techniques," in *2014 9th International* Conference *on Computer Engineering & Systems (ICCES)*, Cairo, Egypt: IEEE, Dec. 2014, pp. 339–345. doi: 10.1109/ICCES.2014.7030983.

[20] J.K. Gómez-Reyes, J.P. Benítez-Rangel, L.A. Morales-Hernández, E. Resendiz-Ochoa, K.A. Camarillo-Gomez, Image mosaicing applied on UAVs survey, *Appl. Sci.* 12 (5) (2022) 2729, https://doi.org/10.3390/app12052729.

[21] N. Yan, et al., Deep learning on image stitching with multi-viewpoint images: a survey, *Neural Process. Lett.* 55 (4) (2023) 3863–3898, https://doi.org/10.1007/s11063-023-11226-z.

[22] E. A. Semenishchev, V. Voronin, A. Zelensky, I. Shraifel, "Algorithm for image stitching in the infrared," in *Infrared Technology and* Applications *XLV*, G. F. Fulop, C. M. Hanson, and B. F. Andresen, Eds., Baltimore, United States: SPIE, May 2019, p. 86. doi: 10.1117/12.2519537.

[23] C. Cai, B. Fan, Q. Zhu, Real-time stitching method for infrared image, *Opt. Eng.* 57 (11) (2018) 1, https://doi.org/10.1117/1.OE.57.11.113103.

[24] C. Yin, X. Huang, X. Tan, J. Liu, "Stitching technique for reconstructed thermal images," in *infrared thermographic NDT-based damage detection and analysis method for spacecraft*, Singapore: Springer Nature Singapore (2024) 93–129, https://doi.org/10.1007/978-981-99-8216-5_4.

[25] H. Zhijian, H. Bingwei, S. Shujin, "An Automatic Image Stitching Method for Infrared Image Series," in *2021 International Conference on* Control, *Automation and Information Sciences (ICCAIS)*, Xi'an, China: IEEE, Oct. 2021, pp. 887–891. doi: 10.1109/ICCAIS52680.2021.9624642.

[26] Yu Wang Mingquan Wang, "Research on stitching technique of medical infrared images," in *2010 International Conference on* Computer *Application and System Modeling (ICCASM 2010)*, Taiyuan, China: IEEE, Oct. 2010, pp. V10-490-V10-493. doi: 10.1109/ICCASM.2010.5622692.

[27] K. Speicher, A. Steinboeck, D. Wild, T. Kiefer, A. Kugi, An integrated thermal model of hot rolling, *Math. Comput. Model. Dyn. Syst.* 20 (1) (2014) 66–86, https://doi.org/10.1080/13873954.2013.809364.

[28] A.E. Jobst, M. Radschun, C. Clemens, A. Hennig, O. Kanoun, J. Himmel, Analysis of the roll imprint on the cross-sectional area of hot rolled wire rod by frequency spectroscopy, *Measurement* 223 (2023) 113755, https://doi.org/10.1016/j.measurement.2023.113755.